



HAL
open science

Structural model for differential cap maturation at growing microtubule ends

Juan Estévez-Gallego, Fernando Josa-Prado, Siou Ku, Ruben Buey, Francisco Balaguer, Andrea Prota, Daniel Lucena-Agell, Christina Kamma-Lorger, Toshiki Yagi, Hiroyuki Iwamoto, et al.

► **To cite this version:**

Juan Estévez-Gallego, Fernando Josa-Prado, Siou Ku, Ruben Buey, Francisco Balaguer, et al.. Structural model for differential cap maturation at growing microtubule ends. *eLife*, 2020, 9, pp.e50155. 10.7554/eLife.50155 . hal-02552246

HAL Id: hal-02552246

<https://hal.science/hal-02552246>

Submitted on 17 Jul 2020

HAL is a multi-disciplinary open access archive for the deposit and dissemination of scientific research documents, whether they are published or not. The documents may come from teaching and research institutions in France or abroad, or from public or private research centers.

L'archive ouverte pluridisciplinaire **HAL**, est destinée au dépôt et à la diffusion de documents scientifiques de niveau recherche, publiés ou non, émanant des établissements d'enseignement et de recherche français ou étrangers, des laboratoires publics ou privés.



Distributed under a Creative Commons Attribution 4.0 International License

Structural model for differential cap maturation at growing microtubule ends

Juan Estévez-Gallego^{1†}, Fernando Josa-Prado^{1†}, Siou Ku^{2†}, Ruben M Buey^{1,3}, Francisco A Balaguer¹, Andrea E Prota⁴, Daniel Lucena-Agell¹, Christina Kamma-Lorger⁵, Toshiki Yagi⁶, Hiroyuki Iwamoto⁷, Laurence Duchesne², Isabel Barasoain¹, Michel O Steinmetz^{4,8}, Denis Chrétien², Shinji Kamimura⁹, J Fernando Díaz¹, Maria A Oliva^{1*}

¹Structural and Chemical Biology Department, Centro de Investigaciones Biológicas, CSIC, Madrid, Spain; ²Univ Rennes, CNRS, IGDR (Institut de Génétique et Développement de Rennes) – UMR 6290, Rennes, France; ³Departamento de Microbiología y Genética, Universidad de Salamanca-Campus Miguel de Unamuno, Salamanca, Spain; ⁴Division of Biology and Chemistry, Laboratory of Biomolecular Research, Paul Scherrer Institut, Villigen, Switzerland; ⁵ALBA synchrotron, CELLS, Cerdanyola del Vallès, Spain; ⁶Department of Life Sciences, Faculty of Life and Environmental Sciences, Prefectural University of Hiroshima, Hiroshima, Japan; ⁷Diffraction and Scattering Division, Japan Synchrotron Radiation Research Institute, Hyogo, Japan; ⁸University of Basel, Biozentrum, Basel, Switzerland; ⁹Department of Biological Sciences, Faculty of Science and Engineering, Chuo University, Tokyo, Japan

*For correspondence:
marian@cib.csic.es

†These authors contributed
equally to this work

Competing interests: The
authors declare that no
competing interests exist.

Funding: See page 21

Received: 12 July 2019
Accepted: 25 January 2020
Published: 10 March 2020

Reviewing editor: Andrew P
Carter, MRC Laboratory of
Molecular Biology, United
Kingdom

© Copyright Estévez-Gallego et al. This article is distributed under the terms of the [Creative Commons Attribution License](https://creativecommons.org/licenses/by/4.0/), which permits unrestricted use and redistribution provided that the original author and source are credited.

Abstract Microtubules (MTs) are hollow cylinders made of tubulin, a GTPase responsible for essential functions during cell growth and division, and thus, key target for anti-tumor drugs. In MTs, GTP hydrolysis triggers structural changes in the lattice, which are responsible for interaction with regulatory factors. The stabilizing GTP-cap is a hallmark of MTs and the mechanism of the chemical-structural link between the GTP hydrolysis site and the MT lattice is a matter of debate. We have analyzed the structure of tubulin and MTs assembled in the presence of fluoride salts that mimic the GTP-bound and GDP•P_i transition states. Our results challenge current models because tubulin does not change axial length upon GTP hydrolysis. Moreover, analysis of the structure of MTs assembled in the presence of several nucleotide analogues and of taxol allows us to propose that previously described lattice expansion could be a post-hydrolysis stage involved in P_i release.

Introduction

Microtubules (MTs) are ubiquitous cytoskeletal polymers built from α/β -tubulin heterodimers that assemble into a pseudo-helical cylinder. They are responsible for essential processes during cell growth and division, including chromosome segregation, intracellular transport, cell support and motility (*Desai and Mitchison, 1997*). MTs perform these functions by serving as scaffolds for other proteins and engaging mechanical forces through their dynamic behavior (*Gigant et al., 2000; Koshland et al., 1988*). Due to its central role in cell biology, tubulin is a reference target for anti-tumor drugs that modulate protein dynamics. Therefore, understanding the molecular mechanisms of tubulin activation and deactivation is crucial to designing more effective compounds that overcome cell resistance and lower the toxicity of compounds in clinical use.

Tubulin exists in two different conformations related to its polymerization state: curved (depolymerized) and straight (assembled into MTs) (*Buey et al., 2006; Gigant et al., 2000;*

Nawrotek et al., 2011; Rice et al., 2008). The binding and hydrolysis of guanosine nucleotides rule the polymerization-depolymerization of tubulin through chemical-linked conformational stages. GDP-tubulin remains inactive in the cytoplasm and the GTP exchange at the exchangeable site (E) on β -tubulin activates the α/β -heterodimers, providing interacting surfaces prone to the addition onto growing bent sheets or protofilaments (PFs) at the MT end (*Chrétien et al., 1995; McIntosh et al., 2018*). The formation of lateral contacts between PFs at the MT tip contributes to tubulin straightening (*Nogales and Wang, 2006*), which is key to creating a hydrolysis competent state (*Nogales et al., 1998; Oliva et al., 2004*). GTP hydrolysis at the E-site in β -tubulin induces conformational changes (*Alushin et al., 2014*) driving the 'peeling-off' disassembly of MTs (*Chrétien et al., 1995; Mandelkow et al., 1991*). MTs' continuous growth and shrinkage generate the motion of these filaments, which is known as dynamic instability (*Mitchison and Kirschner, 1984a*) and involves transient polymer intermediates adopting various nucleotide and conformational states, of which we are getting the first structural glimpses (*Alushin et al., 2014; Zhang et al., 2015; Zhang et al., 2018*). The GDP-bound tubulin forming the body of the MT has a compact, straight and regular lattice, whereas the tip of the MT contains GTP- and GDP•P_i-bound tubulin molecules, and is known as the GTP-cap. This growing MT end varies in size (*Duellberg et al., 2016b*) and decreases in stability with age due to GTP hydrolysis and/or P_i release (*Carlier et al., 1984; Duellberg et al., 2016b; Duellberg et al., 2016a; Gardner et al., 2011; Mitchison and Kirschner, 1984a; Padinhateeri et al., 2012*). The GTP-cap prevents MT depolymerization but its lattice pattern is poorly understood. It has been described as having a tapered shape (*Mandelkow et al., 1991*) or as outwardly curved sheets (*Atherton et al., 2018; Chrétien et al., 1995; Guesdon et al., 2016*), though a recent study suggests flared, curved PFs at growing MT ends (*McIntosh et al., 2018*). It is believed that when GTPase activity reaches the tip and no new capping tubulins are added, MTs switch from growing to shrinking in a multi-step process (*Schek et al., 2007; Walker et al., 1991*) required for the GTP-cap to disappear.

Insight into the nature of the GTP-cap is fundamental to understanding the mechanisms governing MT dynamics and developing new modulating compounds targeting MTs. Here, we address this question using a combination of high- and low-resolution structural techniques with a biochemically controlled in vitro system applied to tubulin and MTs. The use of multiple γ -phosphate analogues (BeF₃⁻, AlF_x) and nucleotides (GMPCPP, GMPPCP, GMPCP) allows us to develop systems that model MTs in their GTP-bound, transitional (GDP•P_i) and metastable (GDP-bound) states. In this model, all tubulin states would be compacted, which contrast with the widely accepted model of an expanded GTP-lattice that would compact after GTP hydrolysis (*Alushin et al., 2014*). We further propose that if previously observed lattice expansion actually occurs during cap maturation, it happens at a post-hydrolysis stage, between the transitional (GDP•P_i) and the metastable GDP-bound states, being an expanded intermediate conformational stage required for P_i release.

Results

Phosphate analogues mimic activation and transition states at the hydrolytic E-site

AlF_x and BeF_x are small inorganic molecules that mimic the chemical structure of phosphate (*Bigay et al., 1987*) and can bind and activate GDP-bound proteins (*Díaz et al., 1997; Mittal et al., 1996*). BeF_x complexes are strictly tetrahedral due to the sp³ orbital hybridization, whereas AlF_x is hexacoordinate (*Coleman et al., 1994; Martin, 1988*) and closely resembles the bipyramidal transition state of phosphate. We combined structural and biochemical studies to validate and correlate the complexes of GDP-tubulin with these γ -phosphate analogues, in both GTP-activated (BeF₃⁻) and GDP•P_i transition (AlF₄⁻/AlF₃) states.

To determine the crystal structure of GDP-tubulin bound to each of the γ -phosphate analogues, we used a tubulin complex with RB3 and TTL (**Figure 1A**), referred to T₂R-TTL (*Prota et al., 2013a*). We included a GDP exchange step during sample preparation (*Díaz and Andreu, 1993*) to ensure the GDP's presence at the E-site. Before setting crystallization plates, we incubated the GDP-T₂R-TTL complexes with either BeF₃⁻ or AlF_x (prepared in situ from mixtures of AlCl₃ and HKF₂ to avoid Al precipitation) to produce GDP-T₂R-TTL-BeF₃⁻ and GDP-T₂R-TTL-AlF_x complexes, respectively. We noticed that BeF₃⁻ and AlF_x cleared easily from the nucleotide binding pocket during crystals

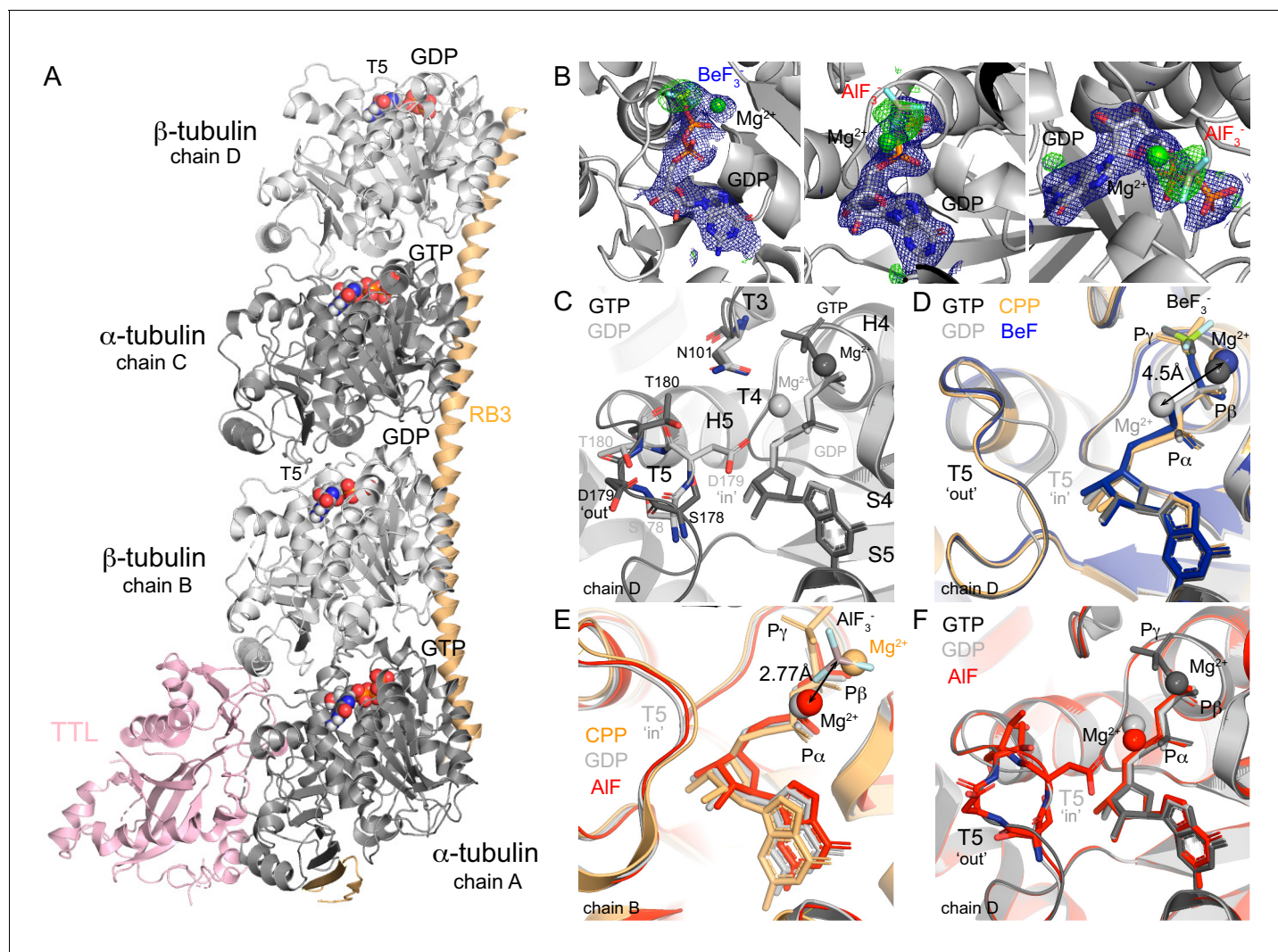


Figure 1. Structure of tubulin bound to GDP-phosphate analogues. (A) The T₂R-TTL complex includes one RB3 molecule (orange), one TTL molecule (pink) and two tubulin heterodimers: α -tubulin (dark gray, GTP-bound, chains A and C), β -tubulin (light gray, GDP-bound, chains B and D). (B) Composite omits maps of BeF₃⁻ (left) and AlF₃ (middle and right): mFo-DFc maps (blue, contour level 1.0) of nucleotide and Mg²⁺ ions combined with 2mFo-DFc maps (green, contour level 3.0) of the related phosphate analogues. (C) GTP (PDB 5xp3, black) and GDP- (PDB 4i55, gray) bound β -tubulin highlighting the localization of secondary structural elements surrounding the nucleotide-binding site according to Löwe *et al.* (2001) and alternative positions of T5 loop depending on the nucleotide-bound state. (D) Chain D alignment of GDP-BeF₃⁻ structure (blue) with GMPCPP-bound (PDB 3ryh, orange), GTP-bound (black) and GDP-bound (gray) structures showing BeF₃⁻/ γ -phosphates co-localization, differences on the position of Mg²⁺ ions depending on the nucleotide-bound state (4.5 Å apart), and T5 loop in a GTP-like ('out') conformation. (E) Chain B alignment of GDP-AlF₃ (red) structure with GMPCPP-bound (orange) and GDP-bound (gray) structures highlighting that AlF₃ sits out of the γ -phosphate site at 2.77 Å from the Mg²⁺ ion (in a position equivalent to that on the GDP-bound structure). (F) Chain D alignment of GDP-AlF₃ (red) structure with GTP-bound (black) and GDP-bound (gray) structures showing the dual conformation of T5 loops.

manipulation, which could be related to their low binding affinity to soluble curved tubulin (see below). After several attempts, we found the BeF₃⁻ and AlF₃ moieties at the E-site of chains D and B (Figure 1A–B), respectively.

The GDP-BeF₃⁻ structure (Table 1, data collection and refinement statistics), shows the phosphate analogue in a tetrahedral state at a distance from the β -phosphate that is similar to the distance observed between the β - and γ -phosphate atoms in the GTP-bound state (Figure 1D), and not further as expected for the transitional GDP•P_i state (Wittinghofer, 1997). Consistent with reported GTP- and GMPCPP-bound tubulin structures, one Mg²⁺ ion coordinates both the β -phosphate and the BeF₃⁻ in a position clearly different than that of GDP-bound tubulin structures (~4.5 Å apart,

Table 1. Data collection and refinement statistics.

	Native T ₂ R-TTL-AlF ₃ (PDB 6s9e)	Native T ₂ R-TTL-BeF ₃ ⁻ (PDB 6gze)
Data collection		
Space group	P2 ₁ 2 ₁ 2 ₁	P2 ₁ 2 ₁ 2 ₁
Cell dimensions		
a, b, c (Å)	104.999, 157.357, 180.261	104.176, 156.744, 180.587
α, β, γ (°)	90.00, 90.00, 90.00	90.00, 90.00, 90.00
Resolution (Å)	48.003–2.25	49.458–2.49
R _{merge}	0.075 (1.222)	0.071 (1.159)
R _{pim}	0.025 (0.417)	0.028 (0.473)
I/σI	16.5 (1.8)	7.1 (0.6)
Completeness (%)	99.0 (99.0)	100 (100)
Redundancy	9.6 (9.2)	7.1 (7.0)
CC _{half}	0.979 (0.635)	0.999 (0.993)
Refinement		
Resolution (Å)	48.003–2.25	49.458–2.49
No. of reflections	140102	103915
R _{work} /R _{free}	0.2029/0.2278	0.2121/0.2565
No. of atoms	17701	16799
Protein	17279	16572
Ligand	223	175
Water	199	52
B-factors		
Protein	64.0	80.4
Ligand	59.5	73.0
Water	45.7	67.5
Wilson B	48.90	64.70
r.m.s deviation		
Bond lengths (Å)	0.002	0.003
Bond angles (°)	0.526	0.557
Ramachandran %		
Favor/allow/out	97.88/2.12/0.00	97.52/2.48/0.00

*Data were collected from a single crystal.

**Values in parentheses are for the highest resolution shell.

Figure 1D). The GDP-BeF₃⁻ complex is stabilized via hydrogen bonds and salt bridges contacts with loops T1, T4, T6 (GDP) and T3 and T4 (BeF₃⁻, **Table 2**). Importantly, loop T5 is in a 'flipped-out' conformation, leaving D179 exposed to the solvent and putting T180 closer to N101 in loop T3 (**Figure 1C–D**) as shown previously in GTP-bound tubulin (**Nawrotek et al., 2011**). Thus, our results suggest that BeF₃⁻ is a γ-phosphate analogue that mimics tubulin's GTP-bound state in the curved conformation, and not a GDP•P_i or intermediate transition state of hydrolysis.

The AlCl₃/HKF₂ mixtures we used produce roughly ~50% AlF₃ and ~50% AlF₄⁻ (**Goldstein, 1964**), and the related moiety was modeled as AlF₃ (**Table 1, Figure 1B**). Strikingly, this analogue did not occupy the position equivalent to the γ-phosphate as observed in other 'classic' GTPase structures of the GDP-AlF₃ complex (e.g. PDB 2ngr, 1grn, 2b92, 2g77, 4jvs and 4iru). Instead, we found the AlF₃ density beside the Mg²⁺ ion (at a distance of 2.77 Å, **Figure 1B**), which was simultaneously coordinating α- and β-phosphates (i.e., GDP coordination, **Figure 1E**, comparison with Mg²⁺

Table 2. PDBePISA analysis of nucleotide-hydrogen bonding at the E-site.

	Curved conformation				Straight conformation					
	GTP (5xp3)	GMPCPP (3ryh)	GDP (4i55)	BeF ₃ ⁻ (6gze)	AlF ₃ (6s9e)	GMPCPP (3jat)	GMPCP (3jal)	GDP (3jar)	GTP-γ-S (3jak)	GDP·P _i (6evx)
Base and ribose	Q11 S140 N206 N228	S140 N228	Q15 N206 N228	N206 N228	N206 N228	N206 Y224 N228	S140 N206 Y224	Q15 S140 N206 Y224	Q15 S140 N206 Y224 N228	S140, N206 N228
Pα	Q11 C12	Q11 C12 S140	C12	C12	C12	Q11 C12	Q11 C12 S140	Q11 C12	C12	C12
Pβ	Q11 G144 T145 G146	Q11 T145 G146	Q11 G144 T145 G146	Q11 G144 T145 G146	Q11 G144 T145 G146	Q11 G144 T145 G146	Q11 G144 T145 G146	Q11 G144 T145 G146	Q11 G144 T145 G146	Q11 G144 T145 G146
Py/ BeF ₃ ⁻ / AlF ₃ / P _i /	A99 G100 N101 G144 T145	A99 G100 N101 G144 T145	-	A99 G100 N101 T145	E71 N101 Pα	A99 G100 G144 T145	-	-	G144 T145	T145
Mg ²⁺	yes	yes	yes	yes	yes	yes	no	no	no	no

positioning of GMPCPP (orange) and GDP (gray) structures). AlF₃ was further stabilized through interactions with loops T2 and T3 and α-phosphate. We hypothesize that this configuration likely represents a transitional stage of P_i release, where the Mg²⁺ ion removes the γ-phosphate while moving to a new coordination position between α- and β-phosphates. Loop T5 in chain B is blocked due to tubulin axial contacts (**Figure 1A**); however, at chain D, this loop refined in a dual conformation during the structure model-building: 57% in GTP-like ‘flip-out’ and 43% in GDP-like ‘flip-in’ conformations (**Figure 1F**, comparison with GTP- (black) and GDP-bound (gray) structures). Since, we did not find any extra density at this chain denoting the presence of the analogue, we presume that very likely the AlF₃ or AlF₄⁻ washed out and we captured loop T5 on its way back to the GDP-bound conformation.

Phosphate analogues induce tubulin activation upon assembly into MTs

We analyzed the effect of γ-phosphate analogues on tubulin activation through time-course turbidity experiments in which we measured the assembly of MTs from fully substituted calf-brain GDP-tubulin in the presence of increasing BeF₃⁻ or AlF_x concentrations (37°C, no GTP added). Notice that our experiments were performed in MES buffer to avoid any competition effect of the commonly used phosphate buffer with the analogues (**Díaz and Andreu, 1993**). In this buffer condition, tubulin assembly requires glycerol under GTP (control experiments) or γ-phosphate analogues conditions, although GMPCPP does not require glycerol to induce assembly. In the presence of BeF₃⁻ GDP-tubulin activation occurred at analogue concentrations above 1 mM (**Figure 2A**), suggesting a binding constant on the scale of mM. The polymerization curves also revealed that longer lag times occur with BeF₃⁻ compared to GTP, indicating that nucleation is less efficient in the presence of GDP-BeF₃⁻. This finding is also supported by the observation of fewer and longer MTs than in GTP control experiments (**Figure 2—figure supplement 1A**). However, we found that the equilibrium constant of addition of a tubulin dimer to the MT end is conserved as is shown by the fact that critical concentration (Cr) values (**Figure 2B**, 3.2 ± 0.4 μM vs. 2.9 ± 0.4 μM in GTP) remained similar across various BeF₃⁻ concentrations. Also, increasing Mg²⁺ concentration had a similar effect on the assembly under GDP-BeF₃⁻ and GTP conditions, displaying similar slopes in the Wyman plot (0.37, **Figure 2C**). Thus, GDP-BeF₃⁻ behaves like a GTP-bound state with slower MT kinetics. Likewise, AlF_x induced tubulin activation with a binding constant in the mM range (**Figure 2D, Figure 2—figure supplement 1B**), which might reflect the fact that part of the molecules had their loop T5 in a GTP-bound conformation according to the crystal structure of AlF₃ tubulin complexes. Previous studies showed similar equilibrium binding constants of addition to the MT, regardless of AlF_x concentration and the clear competition between both AlF_x and BeF₃⁻ for the same site on MTs (**Carlier et al., 1988**). These findings suggest that, (i) both γ-phosphate analogues likely display equivalent biochemical properties and; (ii) AlF_x might occupy the γ-phosphate site on the straight tubulin conformation.

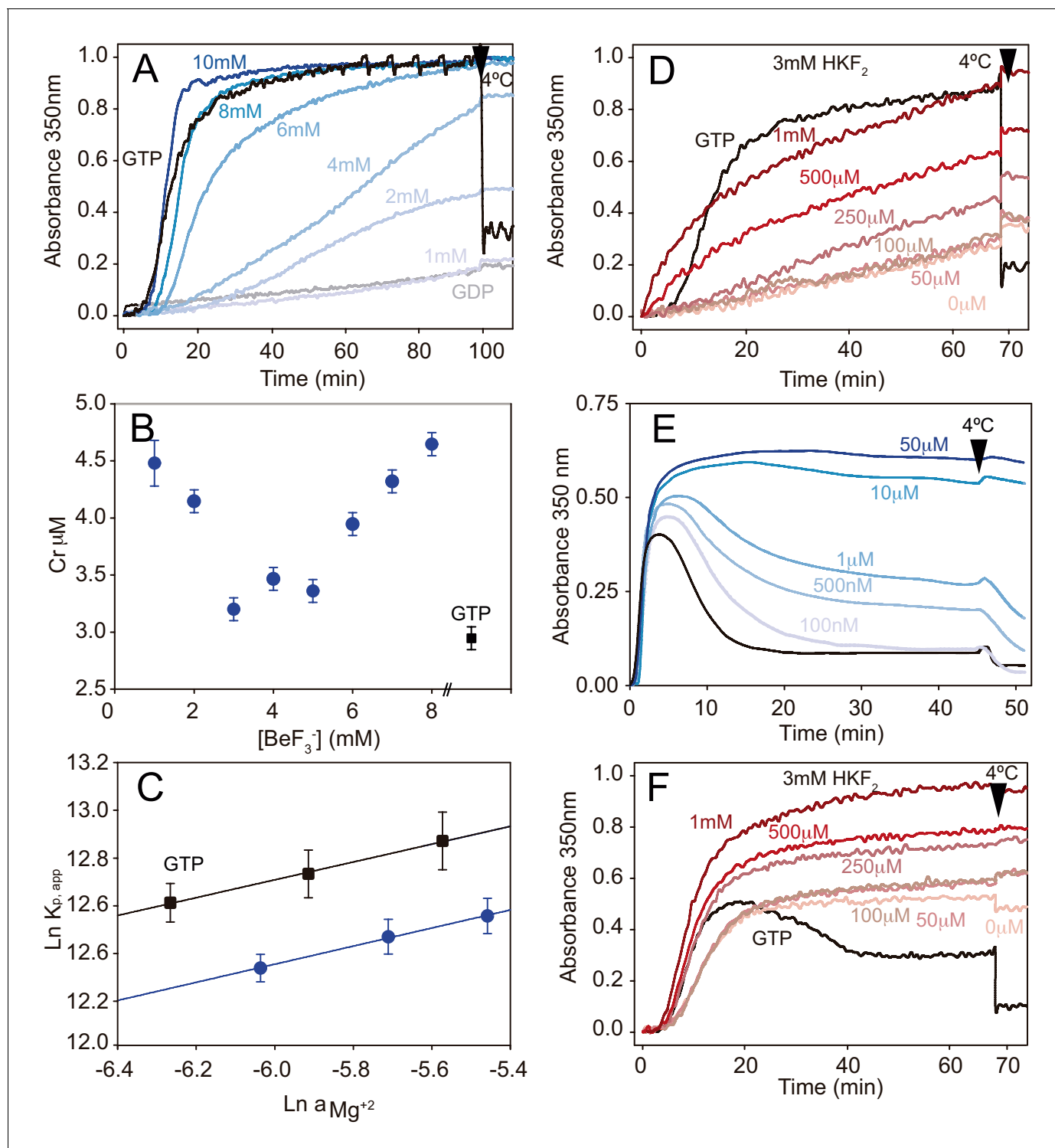


Figure 2. Phosphate analogues sustain tubulin activation and MT stabilization. (A) Time course assembly of 30 μM GDP-tubulin (gray line) with either 1 mM GTP (black line) or 1 mM GDP and increasing BeF_3^- concentrations (1 mM, 2 mM, 4 mM, 6 mM, 8 mM and 10 mM; from light to dark blue). (B) Critical concentration (C_r) measurements of GDP-tubulin with 1 mM GTP (black square) or 1 mM, 2 mM, 3 mM, 4 mM, 5 mM, 6 mM, 7 mM and 8 mM BeF_3^- (blue circles). (C) Wyman plots showing the effect of increasing Mg^{2+} concentrations (4 mM, 5 mM, and 6 mM) on tubulin assembly (37°C) in the presence of 1 mM GTP (black squares) or 1 mM GDP plus 3 mM BeF_3^- (blue circles). Positive slopes indicate that at increasing Mg^{2+} concentrations the ion incorporation into the filament is higher, and similar slope values (under BeF_3^- and GTP) indicate a similar Mg^{2+} dependency of the polymerization. (D) Time course assembly of 30 μM GDP-tubulin with either 1 mM GTP (black line) or 1 mM GDP, 3 mM HKF_2 and increasing concentrations of AlCl_3 (0 μM , 50 μM , 100 μM , 250 μM , 500 μM and 1 mM; from light to dark red). (E) Time course assembly of 30 μM tubulin in the absence of free GTP (black line) and increasing concentrations of AlCl_3 (100 nM, 500 nM, 1 μM , 10 μM , 50 μM and 100 μM ; from light to dark blue). (F) Time course assembly of 30 μM GDP-tubulin with either 1 mM GTP (black line) or 1 mM GDP, 3 mM HKF_2 and increasing concentrations of AlCl_3 (0 μM , 50 μM , 100 μM , 250 μM , 500 μM and 1 mM; from light to dark red). *Figure 2 continued on next page*

Figure 2 continued

line) and in the presence of increasing concentrations of BeF_3^- (100 nM, 500 nM, 1 μM , 10 μM and 50 μM ; from light to dark blue) showing the stabilization effect of the analogue. (F) Time course assembly of 30 μM tubulin in the absence of free GTP and 0 mM HKF_2 (black line) or in the absence of free GTP with 3 mM HKF_2 and increasing concentrations of AlCl_3 (0 μM , 50 μM , 100 μM , 250 μM , 500 μM and 1 mM from light to dark red). Aluminum contamination in nucleotides and glass induce MT stabilization even when no AlCl_3 was added (light red). Arrows in graphs (A), (D), (E), and (F) indicate when samples were incubated at 4°C.

The online version of this article includes the following figure supplement(s) for figure 2:

Figure supplement 1. Electron micrographs of MTs polymerized in the presence of BeF_3^- and AlF_x .

Finally, we verified the effect of these γ -phosphate analogues on the stabilization of MTs assembled in the presence of 30 μM GTP. BeF_3^- inhibits MT disassembly at concentrations between 100–500 nM (**Figure 2E**) and hence, we estimate that the affinity of this γ -phosphate analogue for straight tubulin in assembled MTs (nM range, **Figure 2E**) is about three orders of magnitude higher than that for the curved GDP-bound, soluble protein (mM range, **Figure 2A**). These values correlate with those previously observed for Ras-like small GTPases where the binding affinity of BeF_3^- is in the mM range (**Díaz et al., 1997**), but increases to the μM range with the addition of the GTPase Activating Protein (GAP, **Mittal et al., 1996**). Interestingly, MTs were far more stable at BeF_3^- concentrations > 10 μM (i.e. the depolymerizing effect of non-physiological low temperatures disappeared, **Figure 2E**) likely because BeF_3^- is retained at the γ -phosphate pocket, providing a stable MT conformation in the absence of P_i release. When performing similar experiments to discern AlF_x affinity to straight polymerized tubulin, we found that it is at least two orders of magnitude higher than this for the curved state because MTs were fully stabilized at the lower AlCl_3 concentration we used, 50 μM (**Figure 2F**) and tubulin activation upon assembly still required 0.5 mM AlCl_3 (**Figure 2D**). Unfortunately, Al^{3+} contamination in the glass and nucleotides solutions (**Sternweis and Gilman, 1982**) prevented us from determining the strength of the interaction (**Figure 2F**).

Phosphate analogues reveal lattice features for the GTP/GDP· P_i -bound states

We used X-ray fiber diffraction of aligned filaments in solution to determine the structural details of MTs in various nucleotide-bound states, which gave us the direct correlation between biochemical and structural data. We performed quick shear-flow alignment using methylcellulose (**Sugiyama et al., 2009**) at a constant, physiological temperature of 37°C, which allowed us to avoid temperature-related variations in axial repeat and filament diameter (**Kamimura et al., 2016**). We chose this technique because of the swiftness of getting results related to both the boundaries of the MT wall from the equatorial diffraction, and the axial repeats from the meridional diffraction (**Figure 3—figure supplement 1; Amos and Klug, 1974; Andreu et al., 1992**). Importantly, in these experiments, the signal-to-noise (S/N) ratio for the equatorial signals is very high because data includes the average of tens of millions of individual MTs. Therefore, we have estimated for the first time, the fraction of MT subpopulations according to their number of PFs (**Figure 3—figure supplement 1, Materials and methods**) using the $J_{04} + J_{N1}$ signals.

We first studied MTs polymerized in the presence of either 1 mM GTP (GDP-MTs, due to GTPase activity) or 1 mM GTP + 100 μM taxol (GDP-Tx-MTs) to analyze two known lattice conformations; compacted and expanded (**Alushin et al., 2014; Kellogg et al., 2017**). Under both experimental conditions, we found an axial tubulin repeat of 4 nm (**Figure 3A, lines gray and brown and Figure 3—figure supplement 2**). However, the 1 nm layer line, which is an harmonic of the 4 nm layer line, showed variations on their peaks distribution (**Figure 3A, inset**) indicating differences on the average monomer axial spacing between GDP-MTs and GDP-Tx-MTs. The existence of a second weaker set of ~8 nm layer lines on GDP-Tx-MTs further confirmed variations on the axial spacing between α - and β -tubulin. These experiments did not distinguish between intra-dimer (α - β) and inter-dimer (β - α) distances, but the averaged estimations of monomer lengths are similar to cryo-EM measurements (**Figure 4E**) and published cryo-EM structures (**Alushin et al., 2014; Kellogg et al., 2017**): 4.06 nm vs. 4.01 nm for GDP-MTs and 4.18 nm vs. 4.08 nm for GDP-Tx-MTs. Otherwise, the analysis of the equatorial diffraction showed similar diameters for GDP- and GDP-Tx-MTs (**Table 3,**

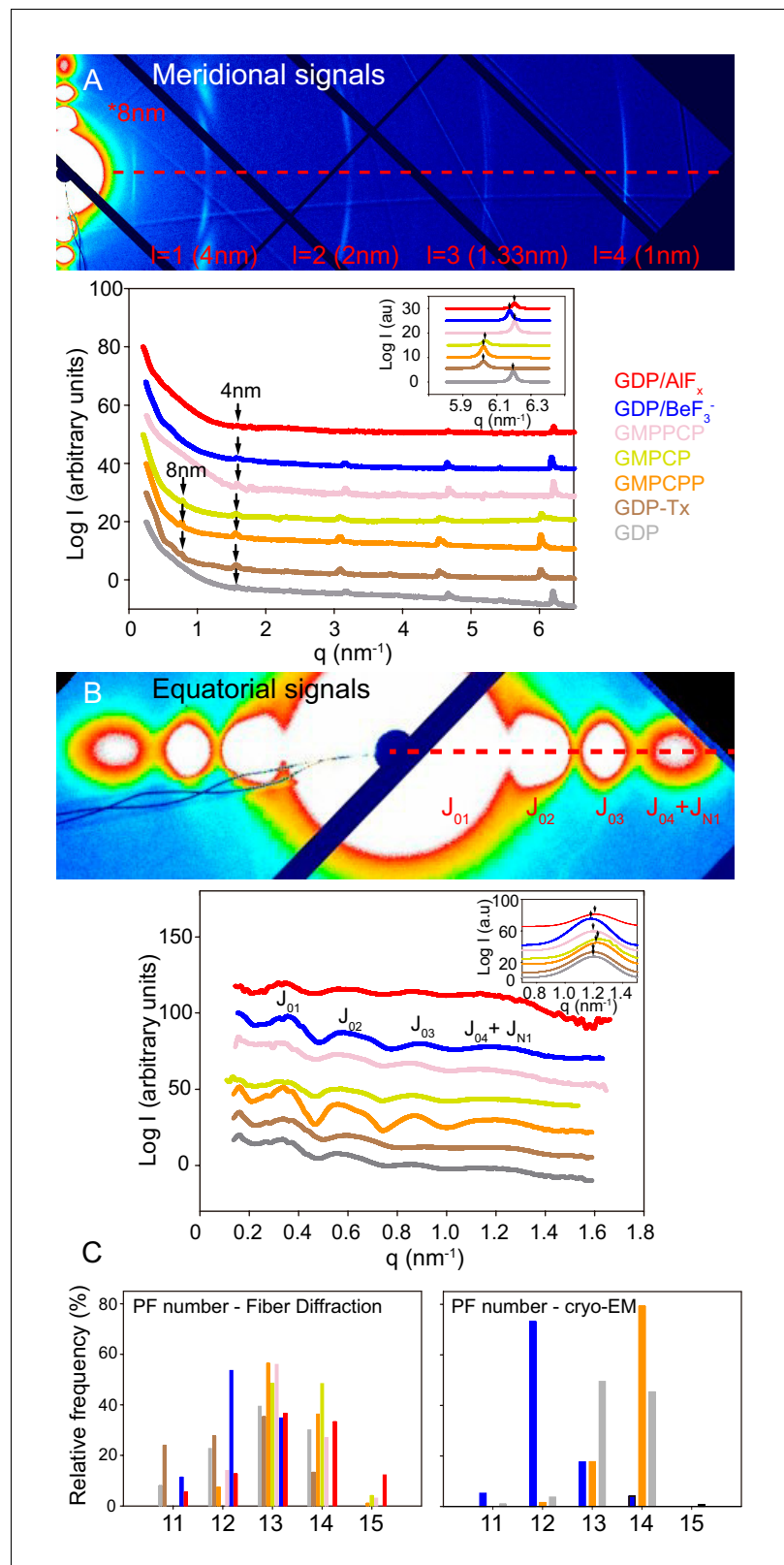


Figure 3. Fiber diffraction of MT models systems. GDP-BeF₃⁻-MT (blue), GDP-AlF_x-MT (red), GMPPCP-MT (salmon), GMPCP-MT (yellow), GMPCPP-MT (orange), GDP-Tx-MT (brown) and GDP-MT (gray). (A) Top; representative image (GMPCPP-MTs) of meridional diffraction displaying the meridional plane from l = 1 (4nm) layer line and related harmonics (l = 2 to 4) for longitudinal metric calculations. Bottom; meridional intensity Figure 3 continued on next page

Figure 3 continued

patterns, where arrows indicate the 4 nm and 8 nm peaks. The inset shows the best fit of 1 nm band experimental intensities in a Lorentzian normal distribution, highlighting positional differences between all tested MT growing conditions (peaks maxima, arrows). (B) *Top*; representative image (GMPCPP-MTs) of equatorial diffraction highlighting the equatorial plane ($l = 0$) for lateral metric calculations. *Bottom*; equatorial intensity patterns showing the corresponding Bessel functions from J_{01} to $J_{04}+J_{N1}$. The inset shows the J_{N1} , calculated as described in M and M, displaying the differences in peak maxima (arrows) that occur under various nucleotide polymerization conditions. The red dash line on (A) and (B) top images shows planes used for intensity line plotting in q_x space and further metric calculations. (C) Estimation of the number of PFs per MT and percentage of each subpopulation within the solution from fiber diffraction experiments (*left*) and cryo-EM images (*right*). The online version of this article includes the following figure supplement(s) for figure 3:

Figure supplement 1. Shear-flow aligned fiber diffraction experiments.

Figure supplement 2. Shear-flow aligned fiber diffraction images.

Figure supplement 3. Shear-flow aligned fiber diffraction images of BeF_3^- - and AlF_x^- -MTs in the presence of taxol.

Figure 3B), although we calculated a slightly different fraction of MT subpopulations according to the number of PFs (**Figure 3C**). The PF number has no effect on the longitudinal spacing (Alushin et al., 2014; Zhang et al., 2015), but does affect the MT helical twist (Chrétien and Wade, 1991). Notice that in our fiber diffracting images the 4 nm layer line is slightly curved, which could be related to the super-twist existing in MTs with skewed PFs (Chrétien and Fuller, 2000). However, we relate this effect to a partial ($2-3^\circ$) misalignment by shearing. Despite such differences, GDP- and GDP-Tx-MTs displayed very alike PFs lateral spacing (**Table 3**), supporting the equivalent lateral contacts found in the aforementioned cryo-EM structures.

Second, we measured the main features of MTs polymerized in the presence of BeF_3^- or AlF_x^- . We analyzed both, MTs polymerized using γ -phosphate analogues (**Figure 2A and D**) as well as MTs assembled from GTP and stabilized by these same salts (**Figure 2E and F**), and found no substantial differences (**Table 3**). Our experiments support that GDP- BeF_3^- mimics the GTP-bound state. In addition, MTs stoichiometrically incorporate Be^7 (Carlier et al., 1988) so, all the subunits within BeF_3^- -MTs must be in the GDP- BeF_3^- state. Strikingly, these MTs did not show the 8 nm layer line (**Figure 3A**, line blue), denoting similar intra-dimer and inter-dimer interfaces (**Table 3**), a clear opposition to the expanded-lattice model of the GTP-bound state displayed by the widely accepted GTP-like analogue, GMPCPP. The fitting of the 1 nm layer line revealed very subtle differences at peak maximum when compared to GDP-MTs, which could suggest minor differences on the axial spacing. The equatorial signals revealed that BeF_3^- -MTs had a slightly smaller diameter and contained fewer average number of PFs than GDP-MTs (**Table 3**), mainly due to the lack of 14- and 15-PF MTs within the estimated population (**Figure 3C**).

AlF_x^- -MTs showed both, close intra-dimer and inter-dimer distances and roughly similar diameters to BeF_3^- -MTs (**Table 3**), suggesting that there is not much of a difference between the GTP- and transition states, either in overall MT dimensions or at the axial interactions. However, AlF_x^- -MTs displayed an additional PF on average (**Table 3**) due to the presence of 14- and 15-PFs MTs.

Tubulin twist in MTs is a consequence of subtle changes in lattice parameters

Cryo-EM was used to get additional details on GDP-, BeF_3^- - and GMPCPP-MTs. Since glycerol at high concentrations is incompatible with cryo-EM and that MT nucleation is difficult in BRB80 buffer in the absence of glycerol, we adopted a seeded assembly strategy. To avoid confusion between GMPCPP- and BeF_3^- lattices, we eluded the use of heterogeneous seeds such as those classically prepared in the presence of GMPCPP. Instead, we first prepared BeF_3^- -MT seeds in the presence of 25% glycerol, which were further diluted 1/10 in tubulin without glycerol. MT assembly was found to be efficient under these conditions (**Figure 4—figure supplement 1**), providing suitable conditions for cryo-EM observations. Importantly, depolymerization at 4°C showed a slower rate with respect to GDP-MTs, comparable to that observed with GMPCPP-MTs, further confirming that BeF_3^- stabilizes MTs (even in a non MES-glycerol buffer, **Figure 2E**).

Consistent with the X-ray diffraction analysis, we found that BeF_3^- -MTs revealed a majority of 12-PFs MTs (73.1%, **Figure 3C**), GDP-MTs contained essentially a mixed population of 13- and 14-PFs

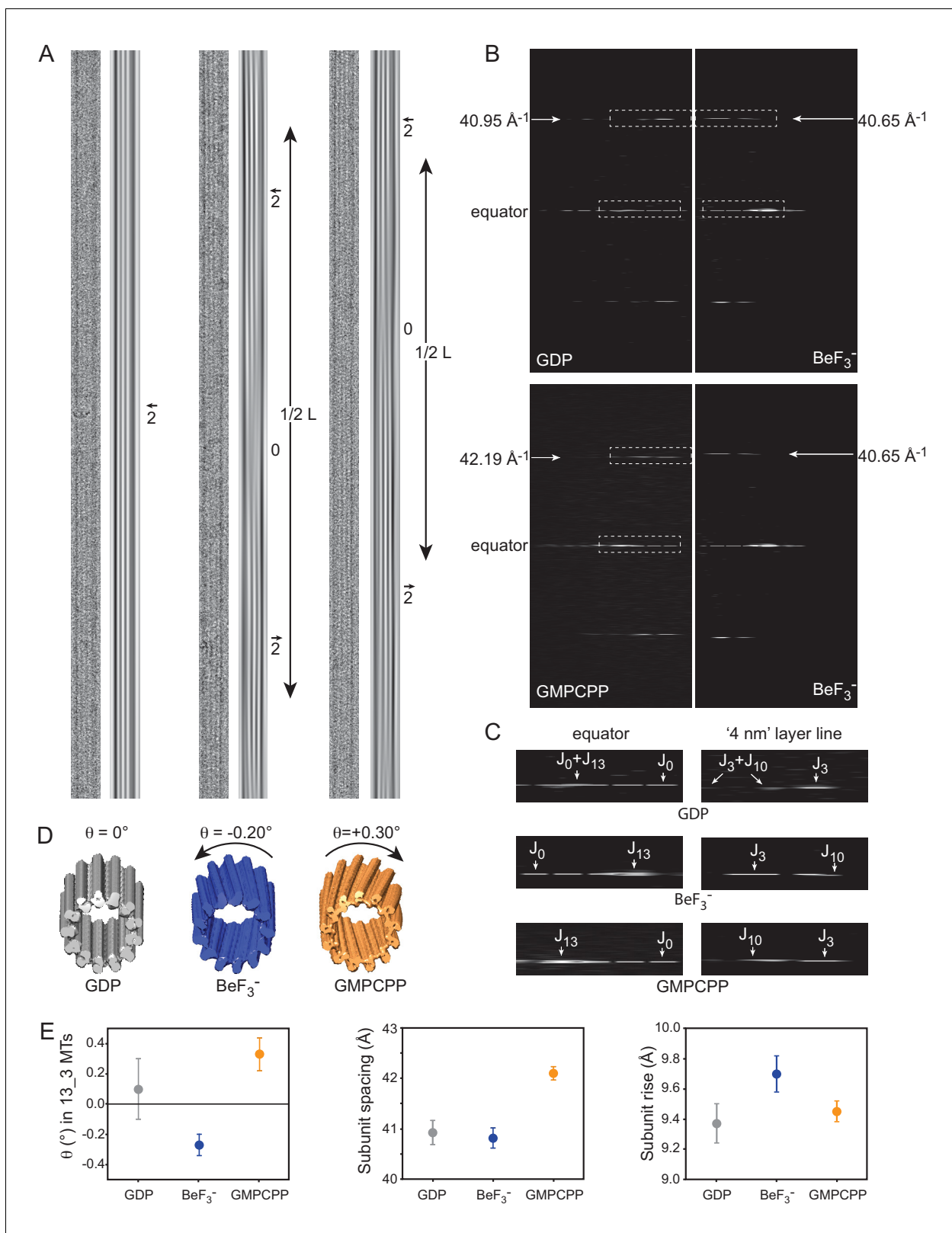


Figure 4. Cryo-EM of GDP-, BeF₃⁻- and GMPCPP-MTs. (A) Straightened images of microtubules with 13 PFs (N) and 3-start monomer helices (S), denoted 13₃ (N_S) MTs. For each condition: raw image (left) and filtered image using the J₀ and J_N layer lines in the FFT of the MTs (right). Filtered images of 13₃ GDP-MTs display 2 dark inner fringes running parallel to the MT axis and slightly offset from it (arrow), which correspond to PFs from the top and bottom surfaces superposed in projection. In BeF₃⁻- and GMPCPP-MTs, the 2 fringes make moiré patterns offset from the MT axis on one

Figure 4 continued on next page

Figure 4 continued

side and the other separated by blurred regions (noted '0' for no internal fringes). The periodicity (L) of these moiré patterns provides a direct measure of their PF skew angle θ (Equation 8). (B) Comparison between the FFTs of the 13_3 GDP- vs. the 13_3 BeF₃⁻-MT (top), and the 13_3 GMPCPP- vs. the 13_3 BeF₃⁻-MT (bottom) in A. The monomer spacing along PFs (a in Equation 9) is given by the position of the J₃ layer line in Fourier space, that is 40.95 Å, 40.65 Å, and 42.19 Å for the 13_3 GDP-, BeF₃⁻- and GMPCPP-MTs in A, respectively. (C) Blow up of the equator and '4 nm layer lines' in 13_3 GDP- (top), BeF₃⁻- (middle) and GMPCPP-MTs (bottom), corresponding to the boxed regions in B. In 13_3 GDP-MTs, J₀ and J_N overlap on the equator, and J₃ and J₁₀ overlap on the '4 nm layer line' since the PFs are parallel to the MT axis. In 13_3 BeF₃⁻- and GMPCPP-MTs, J₁₃ is away from the equator due to the PF skew. In BeF₃⁻-MTs, J₁₀ is closer to the equator than J₃, indicating that the PFs are left-handed (negative skew), while in GMPCPP-MTs, J₁₀ is farther apart from the equator than J₃, indicating that the PFs are right-handed (positive skew), (Chrétien et al., 1996). (D). 3D reconstructions of the 13_3 MTs in A using TubuleJ (Blestel et al., 2009). The 3D reconstructions were elongated to the same size as the original images and presented front face at a slight angle with respect to the MT longitudinal axis to emphasize the PF handedness in 13_3 GDP-MT ($\theta = 0^\circ$), BeF₃⁻-MT ($\theta = -0.20^\circ$), and GMPCPP-MT ($\theta = +0.30^\circ$). (E) Left: average PF skew angles of 13_3 GDP-MTs ($\theta = +0.10 \pm 0.20^\circ$, n = 15), BeF₃⁻-MTs ($\theta = -0.27 \pm 0.07^\circ$, n = 9), and GMPCPP-MTs ($\theta = +0.33 \pm 0.11^\circ$, n = 12). The average PF skew angle of 13_3 GDP-MTs must be lower since a majority of MTs did not show long enough moiré patterns that could be measured at the high magnification used. Therefore, their average PF skew angle is likely closer to 0°. Middle: average monomer spacing along PFs in GDP-MTs (a = 40.93 ± 0.24 Å, n = 66), BeF₃⁻-MTs (a = 40.82 ± 0.20 Å, n = 103), and GMPCPP-MTs (a = 42.10 ± 0.13 Å, n = 25). All N₅ microtubule types were included in the analysis. Right: inter-PF monomer tubulin rise in GDP-MTs (r = 9.37 ± 0.13 Å, n = 64), BeF₃⁻-MTs (r = 9.70 ± 0.12 Å, n = 83), and GMPCPP-MTs (r = 9.45 ± 0.07 Å, n = 24) determined using Equation 9. MTs with modified lateral interactions (essentially observed in 13_4 and 14_4 MTs in BeF₃⁻ conditions) were not included in this analysis (Chrétien and Fuller, 2000). The online version of this article includes the following figure supplement(s) for figure 4:

Figure supplement 1. additional cryo-EM data.

MTs (49.4% and 45.3%, respectively) and GMPCPP-MTs showed mainly 14-PFs MTs (79.2%), which is consistent with previous observations (Hyman et al., 1995). Strikingly, in the presence of BeF₃⁻, 14-PFs MTs were arranged according to 4-start monomer lattices (14_4), and 13-PFs MTs displayed a mixed population of 13_3 and 13_4 MTs (to be reported elsewhere). While 13_3 GDP-MTs had their PFs essentially parallel to the MT axis (Figure 4A, left), both BeF₃⁻- (Figure 4A, middle) and GMPCPP-MTs (Figure 4A, right) displayed systematically moiré patterns, implying that their PFs are skewed relative to the MT axis. Determination of the axial spacing of tubulin monomers from the position of the nominal '4 nm layer line' on the Fourier transform (FFT) of straightened MT images (Figure 4B) confirmed that GDP- and BeF₃⁻-MTs displayed compacted lattices (40.95 Å and 40.65 Å for the MTs in Figure 4A, respectively), while GMPCPP-MTs displayed an extended lattice (42.13 Å for the 13_3 GMPCPP-MT in Figure 4A). Further analysis of the '4 nm layer line' of these MTs (Figure 4C–D) and tilting experiments (not shown) revealed that BeF₃⁻-MTs have left-handed PFs (J₁₀ is closer to the equator than J₃), while GMPCPP-MTs have right handed PFs (J₁₀ is farther apart from the equator than J₃) [Chrétien et al., 1996]. The average PF skew angles of 13_3 GDP-, BeF₃⁻-, and GMPCPP-MTs was found to be +0.10 ± 0.20°, -0.27 ± 0.17°, and +0.33 ± 0.07°, respectively (Figure 4E). These data can be interpreted in light of the lattice accommodation model (Chrétien and Fuller, 2000; Chrétien and Wade, 1991) that describes how the MT lattice accommodates changes in PF and/or helical start numbers, as well as modifications of MT lattice parameters. The theoretical PF skew angle (θ_{the}) of any MT type can be calculated according to Equation 9 (Table 4). While 13_3 GDP-MTs are predicted to have a PF skew close to 0°, an increase of the tubulin monomer spacing a from 40.9 Å to 42.1 Å induces a positive skew of +0.37° similar to that found in GMPCPP-MTs. Likewise, a slight modification of the inter-PF subunit rise r (Equation 10) from

Table 3. Fiber diffraction analysis of MTs in various nucleotide-bound states.

	GDP	GDP-Tx	GDP-BeF ₃ ⁻	GTP-BeF ₃ ⁻	GDP-AIF _x	GTP-AIF _x	GMPCPP	GMPPCP	GMPCP
radius (nm)	11.42 ± 0.10	10.87 ± 0.10	11.21 ± 0.25	11.16 ± 0.10	11.25 ± 0.84	11.18 ± 0.12	11.63 ± 0.10	11.62 ± 0.59	11.75 ± 0.53
avg. PF number	12.91 ± 0.10	12.37 ± 0.10	12.29 ± 0.20	12.23 ± 0.10	13.43 ± 1.12	13.35 ± 0.13	13.29 ± 0.08	13.03 ± 0.91	13.55 ± 0.45
inter-PF distances (nm)	5.50 ± 0.03	5.45 ± 0.01	5.67 ± 0.09	5.67 ± 0.02	5.21 ± 0.46	5.22 ± 0.05	5.45 ± 0.03	5.55 ± 0.38	5.40 ± 0.02
avg. monomer length (nm)	4.06 ± 0.01	4.18 ± 0.01	4.07 ± 0.01	4.07 ± 0.01	4.05 ± 0.05	4.05 ± 0.01	4.18 ± 0.01	4.06 ± 0.01	4.17 ± 0.01
1 nm band peak position (nm ⁻¹)	6.19 ± 0.01	6.02 ± 0.01	6.17 ± 0.01	6.17 ± 0.01	6.20 ± 0.05	6.20 ± 0.01	6.02 ± 0.01	6.20 ± 0.01	6.03 ± 0.01

*Values are Avg ± StdErr.

Table 4. Comparison between experimental and theoretical PF skew angles.

MT type	GDP		BeF ₃ ⁻		GMPCPP	
	13_3	14_3	12_3	13_3	13_3	14_3
θ_{exp}	+0.10 ± 0.21 (n = 15)	-0.62 ± 0.05 (n = 27)	+0.60 ± 0.05 (n = 52)	-0.27 ± 0.07 (n = 9)	+0.33 ± 0.11 (n = 12)	-0.51 ± 0.04 (n = 12)
θ_{the}	+0.05	-0.74	+0.61	-0.31	+0.37	-0.44

Theoretical PF skew angles (θ_{the}) were calculated according to **Equation 9**, using $a = 40.9 \text{ \AA}$, $r = 9.4 \text{ \AA}$, and $\delta x = 48.95 \text{ \AA}$ for GDP-MTs. For GMPCPP MTs, the monomer spacing a was increased to 42.1 \AA , and for BeF₃⁻ the inter-PF subunit rise was increased to 9.7 \AA .

9.37 \AA (GDP-MTs) to 9.70 \AA (BeF₃⁻-MTs) is sufficient to account for the negative PF skew (-0.31°) observed in 13_3 BeF₃⁻-MTs. These features were observed in almost all MTs analyzed in this study (see the 12_3 and 14_3 MTs in **Figure 4—figure supplement 1B–E**), although we note that MTs with large changes in inter-PF rise were also observed in the presence of BeF₃⁻ (essentially 13_4 and 14_4 MTs **Chrétien and Fuller, 2000**). This analysis tells us that the positive PF skew observed in GMPCPP-MTs with respect to GDP-MTs is a simple consequence of the increase in tubulin spacing, most likely due to the presence of the methylene group between the α and β phosphates of GMPCPP (see below), and not a conformational change induced by GMPCPP on tubulin.

MT lattice expansion is not related to its GTP-bound state

GMPCPP has traditionally been considered a good approximation of the GTP-bound state (**Alushin et al., 2014; Hyman et al., 1992; Kamimura et al., 2016; Zhang et al., 2015**), which led to a model in which GTP-tubulin is in an expanded state at the tip of the MTs, and undergoes a compaction followed by rotation between the α and β subunits upon GTP hydrolysis and P_i release, respectively (**Zhang et al., 2015**). Our results suggest that the GTP-state (GDP-BeF₃⁻) is compacted (**Figure 1 and 3**), and that the twist of tubulin in GMPCPP-MTs is a simple consequence of the accommodation of the lattice to the increase in size of GMPCPP-tubulin (**Figure 4, Table 4**). We then asked what was the origin of the increase in size in GMPCPP-tubulin. To address this question, we analyzed the structure of MTs assembled in the presence of GMPPCP that is similar to GMPCPP, but with the methylene group sitting between β and γ phosphates instead of α and β phosphates and GMPCP, which is the hydrolyzed version of GMPCPP. X-ray fiber diffraction analysis of GMPCPP-MTs and GMPPCP-MTs (**Table 3**) highlighted that both GTP analogues generated a similar overall cylinder structure showing equivalent PF number composition in which there were no 11-PF MTs and in which 13- and 14-PF MTs prevailed over 12-PF MTs (**Figure 3C**). GMPCPP-MTs displayed a second set of $\sim 8 \text{ nm}$ layer lines (**Figure 3A, Figure 3—figure supplement 2**), indicating differences between α - and β -tubulin axial spacing, with a monomer repeat that nicely correlates with corresponding measurements from cryo-EM and recently published nude-MT cryo-EM structures (**Zhang et al., 2018**): 4.18 nm vs. 4.22 nm . By contrast, GMPPCP-MTs diffracting images did not show the $\sim 8 \text{ nm}$ layer lines (**Figure 3A, Figure 3—figure supplement 2**) and hence, a non-expanded lattice and a MT structure equivalent to the BeF₃⁻- and GDP-MTs (**Table 3**). Strikingly, the diffraction pattern of GMPCP-MTs was similar to that of GMPCPP-MTs, showing the 8 nm layer line and an expanded state (**Figure 3, Table 3**). Taken all together, these data tell us that: (i) lattice expansion is not related to the presence of γ -phosphate (i.e. a GTP-bound state) and (ii) the methylene in between the α and β phosphates in GMPCPP- and GMPCP-MTs is likely responsible for increasing the size of the tubulin molecule.

We further found that MTs polymerized in the presence of 0.1 mM GTP + $100 \text{ }\mu\text{M}$ taxol showed a nucleotide content of GTP(α):GDP(β), 1.08 ± 0.02 : 1.04 ± 0.01 , similar to other taxane site agents (**Alushin et al., 2014; Field et al., 2018**). Since GTP hydrolysis requires a close intra-dimer distance to fulfill the catalytic pocket (**Nogales et al., 1998; Oliva et al., 2004**), this result suggests that taxol-induced expansion may happen after GTP hydrolysis. Interestingly, we found that BeF₃⁻- and AlF_x-MTs assembled in the presence of $100 \text{ }\mu\text{M}$ taxol displayed compact lattices (**Figure 3—figure supplement 3, Table 5**), bringing up that this drug cannot induce lattice expansion when the interplay between loop T7 and any of these γ -phosphate analogues is retained at the inter-dimer interface.

Table 5. Taxol bound BeF_3^- - and AlF_x -MTs.

	GDP-BeF_3^-	GTP-BeF_3^-	GDP-AlF_x	GTP-AlF_x
Average monomer length (nm)	4.03 ± 0.01	4.03 ± 0.01	4.04 ± 0.05	4.04 ± 0.01
1 nm band peak position (nm^{-1})	6.24 ± 0.01	6.24 ± 0.01	6.22 ± 0.05	6.22 ± 0.01

Discussion

The functions of MTs during cell proliferation and development require continuous rescue and catastrophe events that give rise to motion through dynamic instability. Microtubule-Associated Proteins (MAPs) finely regulate MT function by stabilizing, guiding and destabilizing MT formation, as well as mediating both MT-MT and MT-protein interactions. Plus-end-tracking proteins (+TIPS) are a type of MAP that stabilize or balance MTs; their functions rely on unique structural determinants at the lattice of the MT tip (Maurer et al., 2011; Maurer et al., 2012; Zanic et al., 2009). Thus, understanding these specific structural features is crucial to gain insight into both the mechanisms of MT stabilization and the process of catastrophe.

Incorporation of tubulin dimers into the MT tip forms a cap of not yet hydrolyzed GTP subunits that re-arrange from a naturally bent state to a straight conformation for GTP hydrolysis. The region where this transition occurs is called the GTP-cap, an uneven structure that can extend along hundreds of nanometers (Duellberg et al., 2016b) and ends in an open sheet or flared PFs at the tip (Chrétien et al., 1995; McIntosh et al., 2018). Recent data point to the formation of one lateral contact as the key interaction favoring length-wise PF growth (Mickolajczyk et al., 2019), which occurs 10–50 nm from the growing tip of the PF (~1–7 tubulin heterodimers (Erickson, 2019; McIntosh et al., 2018). Tubulin straightening is not a single step change but a gradual process (Figure 5A), proportional to the increasing formation of lateral interactions in PFs (Brouhard and Rice, 2018; Guesdon et al., 2016; János et al., 1998). In this process, GTPase activity occurs upon tubulin fully-straighten because this unique conformation allows the interplay of the α -tubulin catalytic loop (T7) and the γ -phosphate at the E-site in β -tubulin (Nogales et al., 1998; Oliva et al., 2004), meaning the curled tip might be on the GTP-bound state. However, the transitional nature of GTP-cap architecture is difficult to overcome experimentally. Common approaches include the use of homogeneous model states of the MTs. In this work, we used a broad range of nucleotide-bound model MTs to understand their structure throughout the GTPase cycle (Figure 5A): active upon assembly GTP-bound (GDP-BeF_3^- and GMPPCP), transitional $\text{GDP}\cdot\text{P}_i$ (GDP-AlF_x), metastable GDP (GTP-assembled MTs), and expanded (GMPCPP, GMPCP and GDP-Tx, see below). Our results merge into a cap model (Figure 5B) in which each modeled MT mimics the structural transformations of the filament during elongation, according to the natural biochemical changes caused by GTPase activity.

The existing cap model is based on the commonly accepted GMPCPP analogue as a *bona fide* model of the GTP-bound state and proposes an initial right-handed, expanded lattice (Alushin et al., 2014) that rapidly shrinks and changes twist direction upon hydrolysis during the transition state (exemplified by nude GTP- γ -S-MTs (Zhang et al., 2018) or doublecortin-bound $\text{GDP}\cdot\text{P}_i$ -MTs (Manka and Moores, 2018). GMPCPP induces a far stronger assembly than that from GTP (Hyman et al., 1992), and MTs are stable because this GTP analogue is not easily hydrolysable, despite of a normal oxygen link between β and γ -phosphates. Whether the enhanced activity is due to the lower GTPase rate or the presence of a methylene link between α and β -phosphates is not clear, though it might be related to the expansion because taxol is also a strong tubulin assembly inducer and produces lattice expansion.

Our approach included γ -phosphate analogues that mimic the chemical structure of phosphates on the activation and transitional states, which we structurally and biochemically analyzed on our tubulin system. These data support that, instead of the commonly accepted model, MTs in the GTP-bound state display a compact configuration (Figure 5B, blue). Control experiments with the GTP analogue GMPPCP and with the GDP-analogue GMPCP, confirmed that expansion is due to the presence of the methylene link between α and β -phosphates rather than because of the presence of the γ -phosphate. In our proposed model, the lattice during the transition state of hydrolysis (Figure 5B, red) remains unchanged, despite a possible modification at the inter-PF angle. The

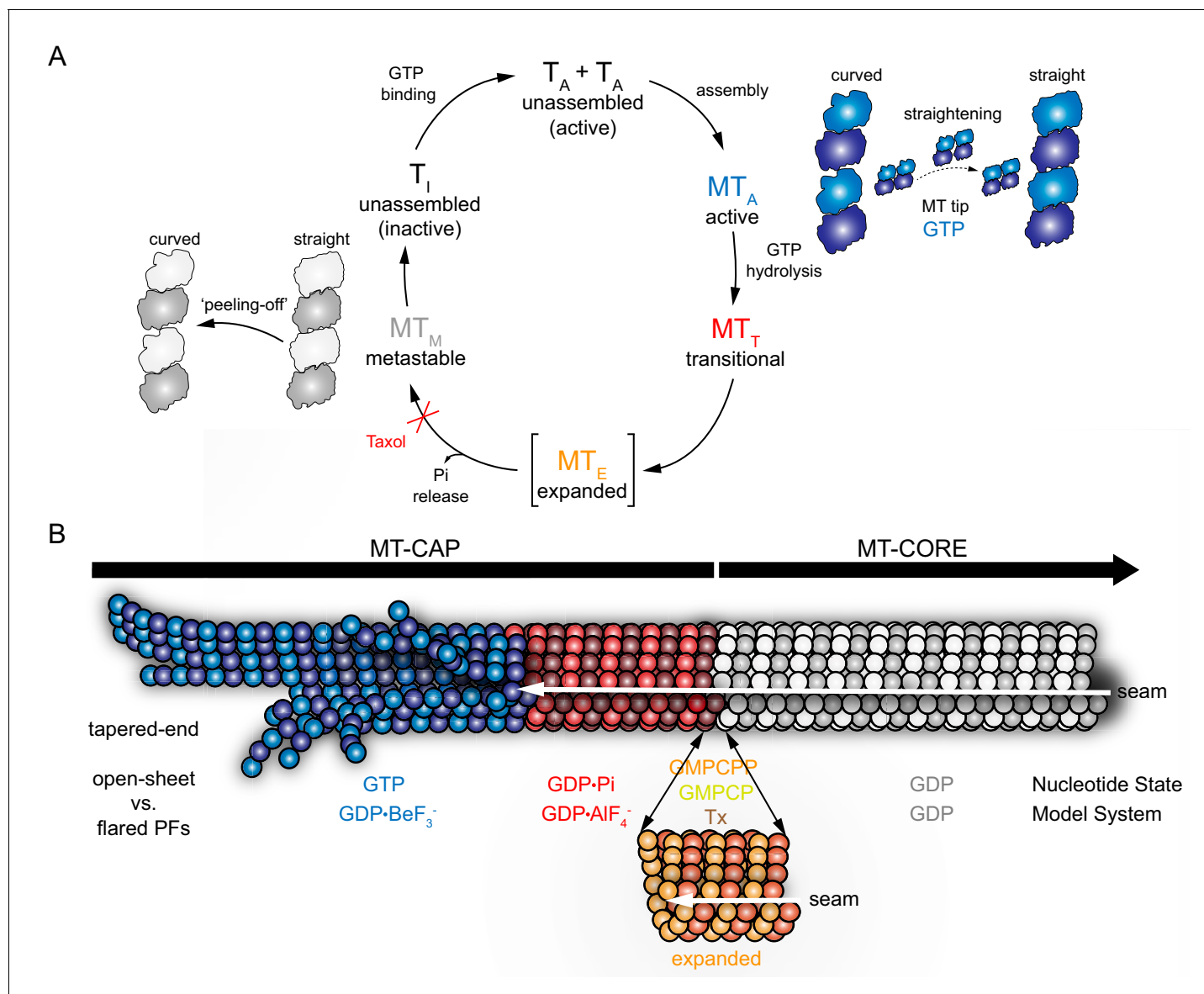


Figure 5. Cap model derived from MT model systems. GTP-bound state (BeF_3^- , blue), transition state (AlF_x , red), expanded state (GMPCPP, GMPCP, $GDP \cdot Tx$, orange), and GDP-bound state (gray). (A) Schematic GTPase related conformational changes within the MT lattice. Tubulin activation upon GTP binding (T_A) induces polymerization. During assembly (MT_A), the formation of lateral contacts favors tubulin straightening, which allows GTP hydrolysis. GTPase activity drives MT through a transitional state (MT_T), where the P_i is at the nucleotide-binding site before it is released. Expansion (orange) may be an intermediate transient step between $GDP \cdot P_i$ and GDP states, which may facilitates P_i release (MT_E) and would be blocked in the presence of taxol. GDP-MT (MT_M) shrinks through a 'peeling-off' disassembly in which tubulin reverts to the curved conformation, which is inactive (T_I) in the GDP-bound state. (B) MT model illustrating specific lattice features of the GTPase cycle. This mosaic structure shows that: (i) the GTP-bound tip (blue) contains curved PFs/sheets that come together into a straight lattice due to the formation of lateral contacts, (ii) the post-hydrolysis $GDP \cdot P_i$ lattice (red) retains overall MT structure, (iii) hypothetically, lattice undergoes an energy-consuming expansion phase (orange) that contributes to P_i release, and (iv) in the GDP state (gray) subtle changes on the PF skew distinguish the metastable compact lattice or, (v) lattice reverts into its previous lower energy state (compaction), preventing the structure from returning to the cap architecture.

$GDP \cdot P_i$ state likely sits between the tapered end and the fully closed, cylindrical end. Its average length is difficult to determine but is considered long according to cap-length estimations made using EB proteins (Duellberg et al., 2016b; Seetapun et al., 2012). Meanwhile, the only difference observed between BeF_3^- and GDP-MTs (Figure 5B, gray) is a slight modification of the PF skew (Figure 4D–E). Therefore, no substantial lattice changes occur between the cap and the MT core

apart from subtle modifications of the PF skew or the displacement of Mg^{2+} ion coordination across β - γ and α - β phosphates.

It should be mentioned that the expanded conformation is not limited to mammalian GMPCPP-, GMPCP- and GDP-Tx-MTs. It also has also been captured in GDP-MTs from yeast and worm (*Chaaban et al., 2018; Howes et al., 2017; von Loeffelholz et al., 2017*), suggesting that this lattice state might not be an artifact. Hence, when or where does this conformational change occur? We propose a plausible explanation considering data arising from the interaction of EB proteins with MTs and recent results on taxanes-binding to the MT cap. EB proteins interact with both, curved and straight regions at MT ends (*Guesdon et al., 2016*), likely recognizing the MT compact lattice, because they bind preferentially to MTs in the presence of $GDP\cdot BeF_3^-$ and $GTP\cdot\gamma$ -S over GMPCPP (*Maurer et al., 2011; Zhang et al., 2015*). Besides, EB proteins form an extended 'comet' that decays exponentially with increasing distance from the tip (*Seetapun et al., 2012*), which highlights their gradual release from the MT wall, with no clue about the structural-chemical determinant inducing such pattern of release. Additionally, it has been shown that fluorescent taxanes bind to the MT region behind the EB 'comet' (*Rai et al., 2019*). From the thermodynamical point of view, if a drug induces a specific conformation, it will bind with higher affinity to this kind of structure, because none of the free energy of binding will be required to induce such conformational change. This implies that taxanes should bind preferentially to expanded lattices because they do induce lattice expansion (*Alushin et al., 2014*). Similarly, EBs might induce lattice compaction (their favored lattice state) in GMPCPP-MTs, causing nucleotide hydrolysis (*Zhang et al., 2018*). Hence, it could be possible that the MT region behind EB-binding site would be expanded, favoring taxanes binding and EBs release. We show that MT lattice is compact among the tubulin GTPase cycle. Therefore, lattice expansion, if existing, might be between two of the main nucleotides bound states (GTP , $GDP\cdot P_i$ and GDP). Since the presence of γ -phosphate analogues (BeF_3^- or AlF_x) reverts taxol-induced expansion (*Figure 5A–B*, orange), we speculate that expansion might be an intermediate state between the MT's cap ($GDP\cdot P_i$) and core (GDP) regions, able to facilitate P_i release (*Figure 5B*). Note that, on the stabilization experiments, the γ -phosphate analogues immediately replace the released P_i and so, no expansion of the compact GDP lattice is needed to justify the biochemical stabilization observed.

Considering the narrow region labeled by these taxanes (*Rai et al., 2019*), it could be argued that lattice expansion might involve only few tubulin molecules likely randomly distributed, which has precluded the detection of expansion on cryo-EM images of the MTs tips. If existing, lattice expansion would be likely the point of no return for the GTP-cap as a stabilizing structure. Thereby, once the MT compacts and returns to the GDP -bound state (*Figure 5B*, gray), the remaining energy stored in the lattice would be enough to exert the peeling-off disassembly of PFs, but below the threshold for the MT to revert to the expanded state. Notice that the 'peeling-off' disassembly is highly efficient and uses only 25% of the energy from the GTPase activity (*Driver et al., 2017; Brouhard and Rice, 2018*).

The GTP-cap is a unique structure that governs MT dynamics; our model depicts a mosaic architecture that undergoes various maturation steps according to tubulin GTPase activity. While GTP binding activates assembly, GTP hydrolysis produces energy, part of which could be used for P_i release, and limits the length of the cap. The presence of an expanded lattice in GDP -MTs of yeast and worm might be a consequence on the delay or inability to return to the compact state, which could be related to the differences observed on lateral contacts between PFs (*Chaaban et al., 2018*). At the moment, we do not know how is the GTP-MT lattice on these organisms and additional studies are necessary to confirm a compact-to-expanded conformational change upon P_i release, although we cannot rule out that MT lattice could be more expanded in other organisms different than mammals. Beyond this study, high-resolution structural studies will be crucial to analyze the exact nature of protein-protein interactions at the tip of the cap and to fully understand the feedback between structural modifications driven by partner proteins that otherwise are regulating MT dynamics.

Accession codes

Data deposition: Atomic coordinates and structure factors for the reported crystal structures have been deposited at the Protein Data Bank under the accession code 6gze (BeF_3^-) and 6s9e (AlF_3).

Materials and methods

Key resources table

Reagent type (species) or resource	Designation	Source or reference	Identifiers	Additional information
Biological Sample	Tubulin alpha	Uniprot	P81947	purified from calf-brain
Biological Sample	Tubulin beta	Uniprot	Q6B856	purified from calf-brain
Gene (<i>Rattus norvegicus</i>)	Stathmin-4	Uniprot	P63043	Overexpression in <i>E. coli</i>
Gene (<i>Gallus gallus</i>)	Tubulin-Tyrosine Ligase	Uniprot	E1BQ43	Overexpression in <i>E. coli</i>
Chemical compound, nucleotide	GMPCPP	Jena Bioscience	Jena Bioscience: GpCpp- NU405	
Chemical compound, nucleotide	GMPPCP	Jena Bioscience	Jena Bioscience: GppCp NU-402	
Chemical compound, nucleotide	GMPCP	Jena Bioscience	Jena Bioscience: GpCp NU-414	
Chemical compound, drug	Taxol	Sigma Aldrich	Sigma Aldrich:T7191	
Software, algorithm	XDS	http://xds.mpimf-heidelberg.mpg.de/	RRID:SCR_015652	
Software, algorithm	AIMLESS	https://www.ccp4.ac.uk/	RRID:SCR_015747	
Software, algorithm	PHASER	https://www.phenix-online.org/documentation/reference/phaser.html	RRID:SCR_014219	
Software, algorithm	PHENIX	https://www.phenix-online.org/	RRID:SCR_016736	
Software, algorithm	COOT	https://www.ccp4.ac.uk/	RRID:SCR_014222	
Software, algorithm	PDBePISA	https://www.ebi.ac.uk/pdbe/pisa/	RRID:SCR_015749	
software, algorithm	ImageJ	https://imagej.nih.gov/ij/	RRID:SCR_003070	
Software, algorithm	XRTtools	BM26-DUBBLE, ESRF		
Software, algorithm	TubuleJ	https://team.inria.fr/serpico/software/tubulej/		

GDP-, GMPCP and GMPPCP-tubulin preparation

Purified calf brain tubulin, and chemicals were as described (*Díaz and Andreu, 1993*). Placlitaxel was from Sigma-Aldrich. GMPCP, GMPCPP and GMPPCP were from Jena Biosciences (Jena, Germany). Nucleotides were analyzed by HPLC as described (*Smith and Ma, 2002*). GMPCP was found to be free of GMPCPP and GTP, and GMPPCP was free of GTP. Fully substituted GDP-tubulin was prepared by a two-step interchange procedure; trehalose, Mg²⁺ and free GTP were removed by size exclusion chromatography in a drained centrifuge column of Sephadex G-25 medium (6 × 1 cm), equilibrated in MEDTA buffer (100 mM MES, 1 mM EDTA, pH 6.7) with 1 mM GDP, at 4°C. GDP up to 10 mM was added to the protein, which was incubated for 30 min on ice. Tubulin was freed of

nucleotide excess and equilibrated in MEDTA buffer with 1 mM GDP by a second chromatography in a cold Sephadex G-25 column (15 × 0.9 cm). The nucleotide content of the protein was quantified by protein precipitation and HPLC as described (Díaz and Andreu, 1993) and was found to be 0.98 ± 0.07 mol GTP/mol tubulin, and 0.99 ± 0.06 mol GDP/mol tubulin. Alternatively fully substituted GDP-tubulin was obtained from GTP-tubulin by hydrolysis. GDP tubulin was equilibrated in a 20 × 1 cm Sephadex G-25 column equilibrated in MEDTA buffer with 3.4 M Glycerol. The nucleotide content of the protein was measured as above and was found to be 0.24 ± 0.02 mol GDP/mol tubulin and 1.75 ± 0.06 mol GTP/mol tubulin. The protein was diluted to 30 μM and supplemented with 6 mM Mg⁺² (final pH 6.5) to induce polymerization into MTs by incubating at 37°C. The assembly was monitored turbidimetrically at 350 nm. Protein assembled into MTs (as checked by electron microscopy) and rapidly disassembled after hydrolysis of the bound nucleotide. Samples were taken at the peak of assembly (Sample A) and after complete disassembly (Sample B). The nucleotide content of the protein was measured as above and was found to be 1.01 ± 0.02 mol GDP/mol tubulin and 0.99 ± 0.03 mol GTP/mol tubulin (Sample A) and 0.96 ± 0.04 mol GDP/mol tubulin and 1.00 ± 0.03 mol GTP/mol tubulin (Sample B). Prior to assembly, tubulin samples were centrifuged at 100,000 g, 4°C, for 10 min using TL100.2 or TL100.4 rotors in a Beckman Optima TLX centrifuge to remove aggregates. GMPCP and GMPPCP tubulin preparation were performed by a two-step protocol based on Mejillano *et al.* (1990). First, 20 mg of lyophilized calf brain tubulin were resuspended in PM buffer (80 mM K-PIPES, 1 mM EGTA, 1 mM dithiothreitol, 0.2 mM Tris, pH 6.8) containing 2 mM GTP and 1.5 mM MgCl₂, in order to get the GDP bound to the protein substituted by GTP due to its higher affinity in the presence of Mg⁺² ions (Correia *et al.*, 1987). Then, the free Mg⁺² and GTP were removed by chromatography in a drained column of Sephadex G-25 (GE Healthcare) (6 × 1 cm), equilibrated in PM buffer containing 50 nM of the desired analogue, two times washing steps by filtration using Amicon MWCO 50 (Merck-Millipore), and concentrated to 700–800 μl. The protein was then passed through 0.45 μm cellulose acetate microfuge column filters (Costar) to remove aggregates. Then 5 mM of the desired nucleotide analogue was added to displace the GTP bound (due to its lower affinity in the absence of Mg⁺²) and the protein was incubated for 30 min at 25°C. The protein was washed and concentrated as before to 600–700 μl and filtered again on a 0.45 μm cellulose acetate microfuge column filter to a final concentration 100–150 μM. After filtration, the protein was HPLC analyzed as described (Smith and Ma, 2002) and was found to be 90% loaded with the desired nucleotide at the E-site. In order to induce MT assembly, tubulin was supplemented with 2 mM GMPCPP, GMPCP or GMPPCP and 3 mM MgCl₂ prior to polymerization.

Crystallization and crystal structure determination

The stathmin-like domain of RB3 and the chicken TTL protein preparations were done as described previously (Prota *et al.*, 2013b; Ravelli *et al.*, 2004). For the T₂R-TTL complex, tubulin (8 mg/mL), TTL (17 mg/mL) and RB3 (26 mg/mL) were mixed and concentrated (Amicon MWCO 10) at 4°C to a final complex concentration of 20 mg/ml. The concentrated mixture was supplemented with 10 mM DTT, 0.1 mM GDP, 1 mM AMPCPP and 5 mM BeF₃⁻ (in T₂RT- BeF₃⁻ complex), or 1.5 mM AlCl₃ and 2 mM HKF₂, or 500 μM AlCl₃, 2 mM HKF₂ (in T₂RT- AlF_x complex), before setting crystallization experiments. Initial crystallization conditions were determined from previous structures (Prota *et al.*, 2014; Prota *et al.*, 2013a; Prota *et al.*, 2016) using the sitting-drop vapor diffusion technique with a reservoir volume of 200 μl and a drop volume of 1 μl of complex and 1 μl of reservoir solution at 20°C. Crystal-producing conditions were further optimized using the hanging drop vapor diffusion method with a reservoir volume of 500 μl and a drop volume of 1 μl of complex and 1 μl of reservoir solution. Native T₂R-TTL-BeF₃⁻ complex was crystallized in 0.1 M MES/0.1 M Imidazole pH 6.5, 0.03 M CaCl₂/0.03 M MgCl₂, 5 mM L-tyrosine, 8.8% glycerol, 5.5% PEG4000. T₂R-TTL-AlF_x complex was crystallized in 0.1 M MES/0.1 M Imidazole pH 6.5, 0.03 M CaCl₂/0.03 M MgCl₂, 5 mM L-tyrosine, 5% glycerol, 5.5% PEG4000 500 μM AlCl₃, 2 mM HKF₂ (alternatively 1.5 mM AlCl₃ and 2 mM HKF₂ were used). Plates were kept at 20°C and crystals appeared within the next 24 hr. Prior flash-cooling in liquid nitrogen, crystals were cryo-protected using 10% PEG4000, increasing glycerol concentrations (16% and 20%), and were supplemented with 7.7 mM BeF₃⁻ or 500 μM AlCl₃ and 2 mM HKF₂ or 1.5 mM AlCl₃ and 2 mM HKF₂ depending on the growing conditions. X-ray diffraction data were collected on beamline ID23-1 of the European Synchrotron Radiation Facility (ESRF) and beamline XALOC of ALBA Synchrotron. Diffraction intensities were indexed and integrated using XDS

(Kabsch, 2010), and scaled using AIMLESS (Winn et al., 2011). Molecular replacement was performed with PHASER (McCoy et al., 2007) using the previously determined structure (PDB 4o2b) as a search model. Structures were completed with cycles of manual building in COOT (Emsley et al., 2010) and refined in PHENIX (Adams et al., 2010), which allowed the determination of alternative conformations on different residues at main chains. Data collection and refinement statistics are summarized in **Table 1**. The ligand interfaces of this structure and other tubulin structures in the curved (PDBs 5xp3, 3ryh, 4i55) or straight (PDBs 3jat, 3jal, 3jar, 3jak, 6ecx) conformations were analyzed using PDBE PISA (Krissinel and Henrick, 2007). Omit maps were calculated in PHENIX using Cartesian annealing and harmonic restraints on the omitted atoms (BeF_3^- or AlF_3).

Microtubule assembly and Cr determination

Tubulin (calf brain purified or fully GDP-exchanged as described above) was exchanged into MEDTA buffer and mixed at a 60:40 ratio with a 8.5 M glycerol, 100 mM MES, 1 mM EDTA buffer pH 6.7 (final buffer concentrations 100 mM MES, 3.4 M glycerol, 1 mM EDTA, 0.6 mM GDP, pH 6.7). These samples were supplemented with MgCl_2 and increasing concentrations of BeF_3^- , 3 mM HKF_2 plus increasing concentrations AlCl_3 , 30 μM GTP plus increasing concentrations of BeF_3^- or 30 μM GTP plus 3 mM HKF_2 plus increasing concentrations of AlCl_3 . The solutions were warmed up to 37°C, and incubated as long as needed to reach polymerization equilibrium. The assembly was monitored by turbidity at a wavelength of 350 nm. Alternatively, the polymers formed were sedimented at 100,000 g for 20 min in a TLA 100 rotor equilibrated at 37°C. Supernatants were separated by aspiration, and pellets were resuspended in a 1% SDS, 10 mM phosphate buffer. Tubulin concentration in pellets and supernatants was measured spectrofluorometrically by excitation at 280 nm and emission at 320 nm (Buey et al., 2005) employing a Shimadzu RF-540 fluorometer (excitation and emission slits, 5 nm) calibrated with standards of known concentration prepared from the same tubulin. Apparent polymer growth equilibrium constants were estimated as the reciprocal of the critical concentrations for polymerization determined at several total protein concentrations (Oosawa, 1975).

MT shear-flow alignment and X-ray fiber diffraction experiments

X-ray fiber diffraction data were collected on beamlines BL11-NDC-SWEET and BL40XU of ALBA (Spain) and SPring-8 (Japan) synchrotrons. Purified bovine brain tubulin (5 mg) was diluted in 500 μL to a final concentration of 100 μM on PM buffer containing 3 mM MgCl_2 and either 2 mM GTP, 0.5 mM GMPCPP, 5 mM GMPCP, 5 mM GMPPCP, 2 mM GTP + 10 mM BeF_3^- , 2 mM GTP + 500 μM AlCl_3 + 2 mM HKF_2 , 2 mM GTP + 200 μM taxol, 2 mM GTP + 10 mM BeF_3^- + 200 μM taxol or 2 mM GTP + 500 μM AlCl_3 + 2 mM HKF_2 + 200 μM taxol. GDP-tubulin was obtained from GTP-tubulin by hydrolysis as described above, and then supplemented with 1 mM GDP + 10 mM BeF_3^- or 1 mM GDP + 500 μM AlCl_3 + 2 mM HKF_2 . All samples were incubated for 20 min at 37°C to induce the maximum fraction of polymerized tubulin, and then were mixed in a 1:1 vol ratio with PM buffer at 3 mM MgCl_2 containing 2% methylcellulose (MO512; Sigma-Aldrich). Final concentration of nucleotides, salts and drugs were 1 mM GTP, 0.25 mM GMPCPP, 2.5 mM GMPCP/GMPPCP, 1 mM GTP + 10 mM BeF_3^- , 1 mM GTP + 500 μM AlCl_3 + 2 mM HKF_2 (salts were not diluted because methylcellulose was further supplemented) and 100 μM taxol. Samples were centrifuged 10 s at 2000 g to eliminate air bubbles and were transferred to the space between a mica disc and a copper plate with a diamond window in the shear-flow device (**Figure 3—figure supplement 1**, (Kamimura et al., 2016; Sugiyama et al., 2009)). The device was kept at 37°C during measurements and the mica disc spun at 10 rps to achieve the shear flow alignment. Several experiments were recorded using different sample-to-detector distances and wavelengths, collecting 150 s exposure time images on a PILATUS3S-1M detector. Background images were acquired in the same conditions, using PM buffer containing 3 mM MgCl_2 with 1% methylcellulose without tubulin. A total of 16–24 diffraction images were averaged for each condition and background subtracted using ImageJ (version 1.51j8; Wayne Rasband, National Institutes of Health, Bethesda, USA). Angular image integrations were performed using the XRTTools software (obtained upon request from beamline BM26-DUBBLE of the ESRF), where the spatial calibration was obtained from Ag-Behenate powder diffraction. For data analysis, we considered MTs as cylinders with a three-start helical pattern. The diffraction pattern of MTs comprises layer lines (l) each defined by a group of Bessel functions of order n . Their structural factor F in the reciprocal space (R) is described by **Equation 1** (Klug et al., 1958):

$$F_{l,n}(R) = J_n(2\pi r_m R) f(R) \quad (1)$$

where J_n is the n^{th} Bessel function, r_m is the radius of a MT with m PFs and $f(R)$ is the structural factor of the sphere defined by **Equation 2** (Malinchik et al., 1997):

$$f(R) = 4\pi r_i^3 \frac{\sin(2\pi r_m R) \cos(2\pi r_m R)}{(2\pi r_m R)^3} \quad (2)$$

This expression is used to include the structural factor of the tubulin wall in the calculation where r_i is the radius of the tubulin monomer considered as a sphere, with a value of 2.48 nm (Kamimura et al., 2016). For radial structural parameters (average MT radius, r_m ; average PF number, m_a ; and average PF distances, d_m), we analyzed the central-equatorial intensity profile ($l = 0$) (**Figure 3—figure supplement 1** blue line). The relationship between diffraction intensity and the structural factor is represented in the expression **Equation 3** (Amos and Klug, 1974; Cochran et al., 1952):

$$\langle I_{l,n}(R) \rangle = |F_{l,n}(R)|^2 \quad (3)$$

The intensity of this layer line $I(R)$ at a reciprocal distance (R) results from a MT mixed population with different PF numbers (m), often from 10 to 15. Considering w_m as the fraction of MTs with m PFs, the resulting intensity was deconvolved as the sum of intensities of individual structure functions $F_{l,n}$ (**Equation 4**)

$$I_{l,n}(R) \langle \rangle = \sum_m w_m \sum_n |F_{l,n}(R)|^2 \quad (4)$$

In the $l = 0$ layer line, diffraction intensity is explained by J_0 and J_n where $n = m$ (Oosawa, 1975). Therefore, from **Equation 4** we obtain the following expression (**Equation 5**):

$$\langle I_{l,m}(R) \rangle = \sum_m w_m (|F_{0,0}(R)|^2 + |F_{0,m}(R)|^2) \quad (5)$$

From **Equation 1** and **Equation 5** we derive the **Equation 6**:

$$\langle I_{l,m}(R) \rangle = \sum_m w_m \left((f(R) J_0(2\pi r_m R))^2 + (f(R) J_m(2\pi r_m R))^2 \right) \quad (6)$$

This equation was used for iterative fitting by least squares of the experimental intensities using the Solver function in Excel (Microsoft, 2010 version). For inter-PF distance determination (d_m), r_m was used as the apothem of an m -apex MT in which the linear distance between them is calculated according to **Equation 7**:

$$d_m(r) = 2r_m \sin\left(\frac{\pi}{m_a}\right) \quad (7)$$

The standard error of these calculated values was determined from the ratio between the experimental maximum intensities values of J_0 and J_n and their standard deviation. For the determination of the average monomer lengths, we analyzed the intensity profile of the central-meridional signals (**Figure 3—figure supplement 1**, red line). The 4th harmonic of the first layer-line ($l = 4$) was fitted to a single-peaked Lorentzian function using Sigma-Plot software (version 12.0), in which the position of the maximum of intensity corresponds to $\frac{1}{4}$ of the average monomer length at the reciprocal space. The standard error was obtained from the standard deviation of the regression applied.

Negative-staining and cryo-electron microscopy

For negative-stain experiments, samples of the assembled tubulin were routinely adsorbed to carbon-coated Formvar films on 300-mesh copper grids, stained in 2% uranyl acetate and observed with a JEOL JEM-1230 at 40,000 K magnification with a digital camera CMOS TVIPS TemCam-F416.

For cryo-EM experiments, tubulin was isolated from porcine brain by two cycles of assembly disassembly (Castoldi and Popov, 2003), followed by a final cycle in the absence of free GTP (Mitchison and Kirschner, 1984b). GDP-tubulin was obtained in BRB80 and stored at -80°C before

use. Spectrophotometry was used to determine suitable conditions for cryo-EM. GDP-MTs were polymerized at a final tubulin concentration of 40 μM in BRB80 (80 mM K-Pipes, 1 mM EGTA, 1 mM Mg^{2+} , pH 6.8 with KOH), 1 mM GTP, 35°C. GMPCPP-MTs were polymerized at 10 μM tubulin concentration in BRB80, 0.1 mM GMPCPP, 35°C. GDP/ BeF_3^- -MTs were assembled using a seeded strategy. GDP/ BeF_3^- -MT seeds were polymerized at 40 μM tubulin concentration in BRB80, 25% glycerol, 20 mM NaF, 5 mM BeSO_4 , 35°C for 1 hr. MTs were sheared by sonication (30 s) followed by up-and-down pipetting, and were diluted 1/10 in pre-warmed tubulin at 40 μM with the same buffer composition but in the absence of glycerol, giving a final glycerol concentration of 2.5% suitable for cryo-EM experiments. The presence of aggregates was checked by switching the temperature to 4°C once the MTs reached steady state. Cryo-EM grids were typically prepared after ~1 hr of assembly. Tobacco Mosaic Virus (TMV) was added to the suspensions before polymerization to be used as internal calibration standards. Four μl samples were pipetted and deposited at the surface of holey-carbon coated grids (R3.5/1, Quantifoil) in an automatic plunge freezer (EM-GP, Leica) under temperature and humidity controlled conditions. Grids were stored in LN_2 before use. Specimen grids were loaded onto a cryo-holder (model 626, Gatan), and were observed in a 200 kV electron microscope (Tecnai G2 Sphera, FEI) equipped with a LaB_6 cathode and a $4\text{k} \times 4\text{k}$ CCD camera (USC4000, Gatan). Images were taken at a nominal magnification of 50,000 X using a $-1.5\ \mu\text{m}$ to $-3\ \mu\text{m}$ defocus range. Images were further calibrated using the 2.3 nm layer line of the TMVs added to the suspensions, which gave a pixel size of $2.16 \pm 0.01\ \text{\AA}$ ($n = 27$). Individual MT images were straightened using TubuleJ (Blestel et al., 2009), which allows a semi-automatic determination of MT centers using the phase information on J_0 in the FFT of the MT images. The PF skew angle ' θ_{exp} ' was determined from the length of the moiré patterns (L , or $1/2 L$ in the case of 13_3 MTs) in the J_0+J_N filtered images of the MTs using:

$$\theta_{exp} = \sin^{-1} \left(\frac{\delta x}{L} \right) \quad (8)$$

where δx denotes the lateral separation between PFs ($\delta x = 48.95\ \text{\AA}$). This latter value was estimated from the increase in MT diameter with PF number in 3D maps of MTs (Sui and Downing, 2010). The sign of θ_{exp} was deduced from the analysis of the respective positions of J_S and J_{N-S} on the '4 nm layer lines' on the FFT of the MT images. Series of tilted images were also used (Chrétien et al., 1996) in cases where the separation between J_S and J_{N-S} was minimal (e.g. 13_3 MTs). The monomer spacing along PFs a was determined from the position of the J_S layer line in the FFT of the MT images (S : monomer helical rise). The theoretical PF skew angle θ_{the} on any N_S MT can be calculated using the following formula (Chrétien and Fuller, 2000):

$$\theta_{the} = \tan^{-1} \left(\frac{1}{\delta x} - \left(\frac{Sa}{N} - r \right) \right) \quad (9)$$

The inter-PF rise r was calculated according to the following formula (Chrétien and Fuller, 2000):

$$r = \frac{Sa}{N} - \frac{\delta x^2}{L \sqrt{1 - \left(\frac{\delta x}{L} \right)^2}} \quad (10)$$

where N denotes the PF number of MTs.

Microtubule nucleotide content

Fully GDP-exchanged tubulin was obtained as described before in MEDTA with 3.4 M Glycerol, 0.1 mM GDP, 6 mM MgCl_2 , pH 6.7. 40 μM GDP-tubulin in the presence of 0.1 mM GTP or 0.1 mM GTP and 50 μM Taxol was incubated at 37°C for 30 min. MTs were sedimented as above and pellets were resuspended in 10 mM phosphate buffer. Nucleotide extraction and HPLC separation were then carried out to determine the concentration of each nucleotide as described (Díaz and Andreu, 1993).

Acknowledgements

We thank Ganadería Fernando Díaz for calf brains supply and staff of beamlines ID23-1 and BM26 (ESRF, Grenoble, France), BL11-NCD-SWEET and XALOC (ALBA, Cerdanyola del Vallès, Spain), and

BL40XU (SPring-8, Japan) for their support. This work was supported by Ministerio de Economía y Competitividad grants BFU2013-47014-P to MAO and BFU2016-75319-R to FDP (both AEI/FEDER, UE); Ministerio de Ciencia e Innovación RYC-2011-07900 to MAO; European Union H2020-MSCA-ITN-ETN/0582 ITN TubInTrain to FDP and AEP; Swiss National Science Foundation (31003A_166608) to MOS; JSPS KAKENHI (16K07328/17H03668) to SK; (FSE) ANR-16-CE11-0017-01 to DC and LD. JE-G was supported by Ministerio de Educación, Cultura y Deporte FPU15-03140 and SK by French Ministry of Higher Education of Research and Innovation (IGDR). Cryo-EM data were acquired on the MRic platform (Univ. Rennes, CNRS, Inserm, BIOSIT-UMS 3480, US_S 018, F-35000 Rennes, France). The authors acknowledge networking contribution by the COST Action CM1407 "Challenging organic syntheses inspired by nature - from natural products chemistry to drug discovery".

Additional information

Funding

Funder	Grant reference number	Author
Ministerio de Economía y Competitividad	BFU2013-47014P	Maria A Oliva
Ministerio de Economía y Competitividad	RYC-2011-07900	Maria A Oliva
Ministerio de Economía y Competitividad	BFU2016-75319-R	J Fernando Díaz
H2020 European Research Council	H2020-MSCA-ITN-EJD-860070	Andrea E Prota J Fernando Díaz
Swiss National Science Foundation	31003A_166608	Michel O Steinmetz
Japan Society for the Promotion of Science	KAKENHI 16K07328/17H03668	Shinji Kamimura
Agence Nationale de la Recherche	ANR-16-C11-0017-01	Denis Chrétien
SPring-8 Proposal	2016B1182	Shinji Kamimura
SPring-8 Proposal	2019B1365	Shinji Kamimura

The funders had no role in study design, data collection and interpretation, or the decision to submit the work for publication.

Author contributions

Juan Estévez-Gallego, Formal analysis, Investigation, Methodology; Fernando Josa-Prado, Isabel Barasoain, Validation, Investigation; Siou Ku, Ruben M Buey, Francisco A Balaguer, Daniel Lucena-Agell, Toshiaki Yagi, Hiroyuki Iwamoto, Formal analysis, Investigation; Andrea E Prota, Funding acquisition, Investigation; Christina Kamma-Lorger, Resources, Investigation; Laurence Duchesne, Conceptualization, Supervision, Funding acquisition; Michel O Steinmetz, Resources, Funding acquisition, Project administration; Denis Chrétien, Conceptualization, Formal analysis, Supervision, Funding acquisition, Writing - review and editing; Shinji Kamimura, Funding acquisition, Investigation, Methodology; J Fernando Díaz, Conceptualization, Formal analysis, Supervision, Funding acquisition, Investigation, Project administration, Writing - review and editing; Maria A Oliva, Conceptualization, Data curation, Formal analysis, Supervision, Funding acquisition, Validation, Investigation, Methodology, Writing - original draft, Project administration, Writing - review and editing

Author ORCIDs

Juan Estévez-Gallego  <http://orcid.org/0000-0003-3889-8488>

Fernando Josa-Prado  <http://orcid.org/0000-0002-6162-3231>

Ruben M Buey  <http://orcid.org/0000-0003-1263-0221>

Denis Chrétien  <https://orcid.org/0000-0001-8261-4396>

J Fernando Díaz  <https://orcid.org/0000-0003-2743-3319>Maria A Oliva  <https://orcid.org/0000-0002-2215-4639>**Decision letter and Author response**Decision letter <https://doi.org/10.7554/eLife.50155.sa1>Author response <https://doi.org/10.7554/eLife.50155.sa2>**Additional files****Supplementary files**

- Transparent reporting form

Data availability

Diffraction data have been deposited in PDB under the accession codes 6gze and 6s9e.

The following datasets were generated:

Author(s)	Year	Dataset title	Dataset URL	Database and Identifier
Oliva MA, Diaz JF	2020	Tubulin-GDP.BeF complex	http://www.rcsb.org/structure/6gze	RCSB Protein Data Bank, 6gze
Oliva MA, Estevez-Gallego J, Diaz JF, Protá AE, Steinmetz MO, Balaguer FA, Lucena-Agell D	2020	Tubulin-GDP.AIF complex	http://www.rcsb.org/structure/6s9e	RCSB Protein Data Bank, 6s9e

The following previously published datasets were used:

Author(s)	Year	Dataset title	Dataset URL	Database and Identifier
Protá AE, Bargsten K, Zurwerra D, Field JJ, Diaz JF, Altmann KH, Steinmetz MO	2012	Crystal structure of tubulin-stathmin-TTL complex	https://www.rcsb.org/structure/4i55	RCSB Protein Data Bank, 4i55
Nawrotek A, Knosow M, Gigant B	2011	GMPCPP-Tubulin: RB3 Stathmin-like domain complex	https://www.rcsb.org/structure/3ryh	RCSB Protein Data Bank, 3ryh
Wang Y, Yang J, Wang T, Chen L	2017	Crystal structure of apo T2R-TTL	https://www.rcsb.org/structure/5xp3	RCSB Protein Data Bank, 5xp3
Zhang R, Nogales E	2015	Cryo-EM structure of GMPCPP-microtubule (14 protofilaments) decorated with kinesin	https://www.rcsb.org/structure/3jat	RCSB Protein Data Bank, 3jat
Zhang R, Nogales E	2015	Cryo-EM structure of GMPCPP-microtubule co-polymerized with EB3	https://www.rcsb.org/structure/3jal	RCSB Protein Data Bank, 3jal
Zhang R, Nogales E	2015	Cryo-EM structure of GDP-microtubule co-polymerized with EB3	https://www.rcsb.org/structure/3jar	RCSB Protein Data Bank, 3jar
Zhang R, Nogales E	2015	Cryo-EM structure of GTPgammaS-microtubule co-polymerized with EB3 (merged dataset with and without kinesin bound)	https://www.rcsb.org/structure/3jak	RCSB Protein Data Bank, 3jak
Manka SW	2017	Cryo-EM structure of GDP.Pi-microtubule rapidly co-polymerised with doublecortin	https://www.rcsb.org/structure/6evx	RCSB Protein Data Bank, 6evx
Nassar N, Hoffman G, Clardy J, Cerione R	1998	TRANSITION STATE COMPLEX FOR GTP HYDROLYSIS BY CDC42: COMPARISONS OF THE HIGH RESOLUTION STRUCTURES FOR CDC42 BOUND TO THE ACTIVE AND CATALYTICALLY	https://www.rcsb.org/structure/2ngr	RCSB Protein Data Bank, 2ngr

COMPROMISED FORMS OF THE CDC42-GAP.

Nassar N, Hoffman GR, Clardy JC, Cerione RA	1998	CRYSTAL STRUCTURE OF THE CDC42/CDC42GAP/ALF3 COMPLEX	https://www.rcsb.org/structure/1grn	RCSB Protein Data Bank, 1grn
Ghosh A, Praefcke GJK, Renault L, Wittinghofer A, Herrmann C	2005	Crystal-structure of the N-terminal Large GTPase Domain of human Guanylate Binding protein 1 (hGBP1) in complex with GDP/ALF3	https://www.rcsb.org/structure/2b92	RCSB Protein Data Bank, 2b92
Pan X, Eathiraj S, Munson M, Lamb-right DG	2007	Crystal Structure of Gyp1 TBC domain in complex with Rab33 GTPase bound to GDP and ALF3	https://www.rcsb.org/structure/2g77	RCSB Protein Data Bank, 2g77
Yu Q, Yao Q, Wang D-C, Shao F	2013	Crystal structure of LepB GAP domain from Legionella drancourtii in complex with Rab1-GDP and ALF3	https://www.rcsb.org/structure/4jvs	RCSB Protein Data Bank, 4jvs
Mishra AK, Del-campo CM, Collins RE, Roy CR, Lambricht DG	2013	Crystal Structure of lepB GAP core in a transition state mimetic complex with Rab1A and ALF3	https://www.rcsb.org/structure/4iru	RCSB Protein Data Bank, 4iru

References

- Adams PD**, Afonine PV, Bunkóczi G, Chen VB, Davis IW, Echols N, Headd JJ, Hung LW, Kapral GJ, Grosse-Kunstleve RW, McCoy AJ, Moriarty NW, Oeffner R, Read RJ, Richardson DC, Richardson JS, Terwilliger TC, Zwart PH. 2010. PHENIX: a comprehensive Python-based system for macromolecular structure solution. *Acta Crystallographica Section D Biological Crystallography* **66**:213–221. DOI: <https://doi.org/10.1107/S0907444909052925>, PMID: 20124702
- Alushin GM**, Lander GC, Kellogg EH, Zhang R, Baker D, Nogales E. 2014. High-Resolution microtubule structures reveal the structural transitions in $\alpha\beta$ -Tubulin upon GTP hydrolysis. *Cell* **157**:1117–1129. DOI: <https://doi.org/10.1016/j.cell.2014.03.053>
- Amos L**, Klug A. 1974. Arrangement of subunits in flagellar microtubules. *Journal of Cell Science* **14**:523–549. PMID: 4830832
- Andreu JM**, Bordas J, Díaz JF, García de Ancos J, Gil R, Medrano FJ, Nogales E, Pantos E, Towns-Andrews E. 1992. Low resolution structure of microtubules in solution. Synchrotron X-ray scattering and electron microscopy of taxol-induced microtubules assembled from purified tubulin in comparison with glycerol and MAP-induced microtubules. *Journal of Molecular Biology* **226**:169–184. DOI: [https://doi.org/10.1016/0022-2836\(92\)90132-4](https://doi.org/10.1016/0022-2836(92)90132-4), PMID: 1352357
- Atheton J**, Stouffer M, Francis F, Moores CA. 2018. Microtubule architecture in vitro and in cells revealed by cryo-electron tomography. *Acta Crystallographica Section D* **74(Pt 6)**:572–584. DOI: <https://doi.org/10.1107/S2059798318001948>
- Bigay J**, Deterre P, Pfister C, Chabre M. 1987. Fluoride complexes of aluminium or beryllium act on G-proteins as reversibly bound analogues of the gamma phosphate of GTP. *The EMBO Journal* **6**:2907–2913. DOI: <https://doi.org/10.1002/j.1460-2075.1987.tb02594.x>, PMID: 2826123
- Blestel S**, Kervrann C, Chrétien D. 2009. A Fourier-Based Method for Detecting Curved Microtubule Centers: Application to Straightening of Cryo-Electron Microscope Images. Proceedings / IEEE International Symposium on Biomedical Imaging: from nano to macro. IEEE International Symposium on Biomedical Imaging. DOI: <https://doi.org/10.1109/ISBI.2009.5193043>
- Brouhard GJ**, Rice LM. 2018. Microtubule dynamics: an interplay of biochemistry and mechanics. *Nature Reviews Molecular Cell Biology* **19**:451–463. DOI: <https://doi.org/10.1038/s41580-018-0009-y>, PMID: 29674711
- Buey RM**, Barasoain I, Jackson E, Meyer A, Giannakakou P, Paterson I, Mooberry S, Andreu JM, Díaz JF. 2005. Microtubule interactions with chemically diverse stabilizing agents: thermodynamics of binding to the paclitaxel site predicts cytotoxicity. *Chemistry & Biology* **12**:1269–1279. DOI: <https://doi.org/10.1016/j.chembiol.2005.09.010>, PMID: 16356844
- Buey RM**, Díaz JF, Andreu JM. 2006. The nucleotide switch of tubulin and microtubule assembly: a polymerization-driven structural change. *Biochemistry* **45**:5933–5938. DOI: <https://doi.org/10.1021/bi060334m>, PMID: 16681364
- Carlier MF**, Hill TL, Chen Y. 1984. Interference of GTP hydrolysis in the mechanism of microtubule assembly: an experimental study. *PNAS* **81**:771–775. DOI: <https://doi.org/10.1073/pnas.81.3.771>, PMID: 6583675
- Carlier MF**, Didry D, Melki R, Chabre M, Pantaloni D. 1988. Stabilization of microtubules by inorganic phosphate and its structural analogs, the fluoride complexes of aluminum and beryllium. *Biochemistry* **27**:3555–3559. DOI: <https://doi.org/10.1021/bi00410a005>
- Castoldi M**, Popov AV. 2003. Purification of brain tubulin through two cycles of polymerization-depolymerization in a high-molarity buffer. *Protein Expression and Purification* **32**:83–88. DOI: [https://doi.org/10.1016/S1046-5928\(03\)00218-3](https://doi.org/10.1016/S1046-5928(03)00218-3), PMID: 14680943

- Chaaban S**, Jariwala S, Hsu C-T, Redemann S, Kollman JM, Müller-Reichert T, Sept D, Bui KH, Brouhard GJ. 2018. The structure and dynamics of *C. elegans* Tubulin Reveals the Mechanistic Basis of Microtubule Growth. *Developmental Cell* **47**:191–204. DOI: <https://doi.org/10.1016/j.devcel.2018.08.023>
- Chrétien D**, Fuller SD, Karsenti E. 1995. Structure of growing microtubule ends: two-dimensional sheets close into tubes at variable rates. *The Journal of Cell Biology* **129**:1311–1328. DOI: <https://doi.org/10.1083/jcb.129.5.1311>, PMID: 7775577
- Chrétien D**, Kenney JM, Fuller SD, Wade RH. 1996. Determination of microtubule polarity by cryo-electron microscopy. *Structure* **4**:1031–1040. DOI: [https://doi.org/10.1016/S0969-2126\(96\)00110-4](https://doi.org/10.1016/S0969-2126(96)00110-4), PMID: 8805589
- Chrétien D**, Fuller SD. 2000. Microtubules switch occasionally into unfavorable configurations during elongation. *Journal of Molecular Biology* **298**:663–676. DOI: <https://doi.org/10.1006/jmbi.2000.3696>, PMID: 10788328
- Chrétien D**, Wade RH. 1991. New data on the microtubule surface lattice. *Biology of the Cell* **71**:161–174. DOI: [https://doi.org/10.1016/0248-4900\(91\)90062-R](https://doi.org/10.1016/0248-4900(91)90062-R), PMID: 1912942
- Cochran W**, Crick FH, Vand V. 1952. The structure of synthetic polypeptides. I. the transform of atoms on a Helix. *Acta Crystallographica* **5**:581–586. DOI: <https://doi.org/10.1107/S0365110X52001635>
- Coleman DE**, Berghuis AM, Lee E, Linder ME, Gilman AG, Sprang SR. 1994. Structures of active conformations of α 1 and the mechanism of GTP hydrolysis. *Science* **265**:1405–1412. DOI: <https://doi.org/10.1126/science.8073283>, PMID: 8073283
- Correia JJ**, Baty LT, Williams RC. 1987. Mg²⁺ dependence of guanine nucleotide binding to tubulin. *The Journal of Biological Chemistry* **262**:17278–17284. PMID: 2826416
- Desai A**, Mitchison TJ. 1997. Microtubule polymerization dynamics. *Annual Review of Cell and Developmental Biology* **13**:83–117. DOI: <https://doi.org/10.1146/annurev.cellbio.13.1.83>, PMID: 9442869
- Díaz JF**, Sillen A, Engelborghs Y. 1997. Equilibrium and kinetic study of the conformational transition toward the active state of p21Ha^{ras}, induced by the binding of BeF₃- to the GDP-bound state, in the absence of GTPase-activating proteins. *The Journal of Biological Chemistry* **272**:23138–23143. DOI: <https://doi.org/10.1074/jbc.272.37.23138>, PMID: 9287316
- Díaz JF**, Andreu JM. 1993. Assembly of purified GDP-tubulin into microtubules induced by taxol and taxotere: reversibility, ligand stoichiometry, and competition. *Biochemistry* **32**:2747–2755. DOI: <https://doi.org/10.1021/bi00062a003>, PMID: 8096151
- Driver JW**, Geyer EA, Bailey ME, Rice LM, Asbury CL. 2017. Direct measurement of conformational strain energy in protofilaments curling outward from disassembling microtubule tips. *eLife* **6**:e28433. DOI: <https://doi.org/10.7554/eLife.28433>, PMID: 28628007
- Duellberg C**, Cade NI, Surrey T. 2016a. Microtubule aging probed by microfluidics-assisted tubulin washout. *Molecular Biology of the Cell* **27**:3563–3573. DOI: <https://doi.org/10.1091/mbc.e16-07-0548>, PMID: 27489342
- Duellberg C**, Cade NI, Holmes D, Surrey T. 2016b. The size of the EB cap determines instantaneous microtubule stability. *eLife* **5**:e13470. DOI: <https://doi.org/10.7554/eLife.13470>, PMID: 27050486
- Emsley P**, Lohkamp B, Scott WG, Cowtan K. 2010. Features and development of coot. *Acta Crystallographica. Section D, Biological Crystallography* **66**:486–501. DOI: <https://doi.org/10.1107/S0907444910007493>, PMID: 20383002
- Erickson HP**. 2019. Microtubule assembly from single flared Protofilaments-Forget the cozy corner? *Biophysical Journal* **116**:2240–2245. DOI: <https://doi.org/10.1016/j.bpj.2019.05.005>, PMID: 31122668
- Field JJ**, Pera B, Gallego JE, Calvo E, Rodríguez-Salarichs J, Sáez-Calvo G, Zuwerra D, Jordi M, Andreu JM, Prota AE, Ménchon G, Miller JH, Altmann KH, Díaz JF. 2018. Zampanolide binding to tubulin indicates Cross-Talk of taxane site with colchicine and nucleotide sites. *Journal of Natural Products* **81**:494–505. DOI: <https://doi.org/10.1021/acs.jnatprod.7b00704>, PMID: 29023132
- Gardner MK**, Zanic M, Gell C, Bormuth V, Howard J. 2011. Depolymerizing kinesins Kip3 and MCAK shape cellular microtubule architecture by differential control of catastrophe. *Cell* **147**:1092–1103. DOI: <https://doi.org/10.1016/j.cell.2011.10.037>, PMID: 22118464
- Gigant B**, Curmi PA, Martin-Barbey C, Charbaut E, Lachkar S, Lebeau L, Siavoshian S, Sobel A, Knossow M. 2000. The 4 Å X-ray structure of a tubulin:stathmin-like domain complex. *Cell* **102**:809–816. DOI: [https://doi.org/10.1016/S0092-8674\(00\)00069-6](https://doi.org/10.1016/S0092-8674(00)00069-6), PMID: 11030624
- Goldstein G**. 1964. Equilibrium distribution of Metal-Fluoride complexes. *Analytical Chemistry* **36**:243–244. DOI: <https://doi.org/10.1021/ac60207a074>
- Guesdon A**, Bazile F, Buey RM, Mohan R, Monier S, García RR, Angevin M, Heichette C, Wieneke R, Tampé R, Duchesne L, Akhmanova A, Steinmetz MO, Chrétien D. 2016. EB1 interacts with outwardly curved and straight regions of the microtubule lattice. *Nature Cell Biology* **18**:1102–1108. DOI: <https://doi.org/10.1038/ncb3412>, PMID: 27617931
- Howes SC**, Geyer EA, LaFrance B, Zhang R, Kellogg EH, Westermann S, Rice LM, Nogales E. 2017. Structural differences between yeast and mammalian microtubules revealed by cryo-EM. *The Journal of Cell Biology* **216**:2669–2677. DOI: <https://doi.org/10.1083/jcb.201612195>, PMID: 28652389
- Hyman AA**, Salsler S, Drechsel DN, Unwin N, Mitchison TJ. 1992. Role of GTP hydrolysis in Microtubule dynamics: information from a slowly hydrolyzable analogue, GMPCPP. *Molecular Biology of the Cell* **3**:1155–1167. DOI: <https://doi.org/10.1091/mbc.3.10.1155>, PMID: 1421572
- Hyman AA**, Chrétien D, Arnal I, Wade RH. 1995. Structural changes accompanying GTP hydrolysis in microtubules: information from a slowly hydrolyzable analogue guanylyl-(α,β)-methylene-diphosphonate. *The Journal of Cell Biology* **128**:117–125. DOI: <https://doi.org/10.1083/jcb.128.1.117>
- Jánosí IM**, Chrétien D, Flyvbjerg H. 1998. Modeling elastic properties of microtubule tips and walls. *European Biophysics Journal* **27**:501–513. DOI: <https://doi.org/10.1007/s002490050160>, PMID: 9760731

- Kabsch W.** 2010. Xds. *Acta Crystallogr D Biol Crystallogr D* **66**(Pt 2):125–132. DOI: <https://doi.org/10.1107/S0907444909047337>
- Kamimura S,** Fujita Y, Wada Y, Yagi T, Iwamoto H. 2016. X-ray fiber diffraction analysis shows dynamic changes in axial tubulin repeats in native microtubules depending on paclitaxel content, temperature and GTP-hydrolysis. *Cytoskeleton* **73**:131–144. DOI: <https://doi.org/10.1002/cm.21283>, PMID: 26873786
- Kellogg EH,** Hejab NMA, Howes S, Northcote P, Miller JH, Díaz JF, Downing KH, Nogales E. 2017. Insights into the distinct mechanisms of action of taxane and Non-Taxane microtubule stabilizers from Cryo-EM structures. *Journal of Molecular Biology* **429**:633–646. DOI: <https://doi.org/10.1016/j.jmb.2017.01.001>, PMID: 28104363
- Klug A,** Crick FHC, Wyckoff HW. 1958. Diffraction by helical structures. *Acta Crystallographica* **11**:199–213. DOI: <https://doi.org/10.1107/S0365110X58000517>
- Koshland DE,** Mitchison TJ, Kirschner MW. 1988. Polewards chromosome movement driven by microtubule depolymerization in vitro. *Nature* **331**:499–504. DOI: <https://doi.org/10.1038/331499a0>, PMID: 3340202
- Krissinel E,** Henrick K. 2007. Inference of macromolecular assemblies from crystalline state. *Journal of Molecular Biology* **372**:774–797. DOI: <https://doi.org/10.1016/j.jmb.2007.05.022>, PMID: 17681537
- Löwe J,** Li H, Downing KH, Nogales E. 2001. Refined structure of alpha beta-tubulin at 3.5 Å resolution. *Journal of Molecular Biology* **313**:1045–1057. DOI: <https://doi.org/10.1006/jmbi.2001.5077>, PMID: 11700061
- Malinchik S,** Xu S, Yu LC. 1997. Temperature-induced structural changes in the myosin thick filament of skinned rabbit psoas muscle. *Biophysical Journal* **73**:2304–2312. DOI: [https://doi.org/10.1016/S0006-3495\(97\)78262-6](https://doi.org/10.1016/S0006-3495(97)78262-6), PMID: 9370427
- Mandelkow EM,** Mandelkow E, Milligan RA. 1991. Microtubule dynamics and microtubule caps: a time-resolved cryo-electron microscopy study. *The Journal of Cell Biology* **114**:977–991. DOI: <https://doi.org/10.1083/jcb.114.5.977>, PMID: 1874792
- Manka SW,** Moores CA. 2018. The role of tubulin-tubulin lattice contacts in the mechanism of microtubule dynamic instability. *Nature Structural & Molecular Biology* **25**:607–615. DOI: <https://doi.org/10.1038/s41594-018-0087-8>, PMID: 29967541
- Martin RB.** 1988. Ternary hydroxide complexes in neutral solutions of Al³⁺ and F⁻. *Biochemical and Biophysical Research Communications* **155**:1194–1200. DOI: [https://doi.org/10.1016/S0006-291X\(88\)81266-X](https://doi.org/10.1016/S0006-291X(88)81266-X), PMID: 3178801
- Maurer SP,** Bieling P, Cope J, Hoenger A, Surrey T. 2011. GTPγS microtubules mimic the growing microtubule end structure recognized by end-binding proteins (EBs). *PNAS* **108**:3988–3993. DOI: <https://doi.org/10.1073/pnas.1014758108>, PMID: 21368119
- Maurer SP,** Fourniol FJ, Bohner G, Moores CA, Surrey T. 2012. EBs recognize a nucleotide-dependent structural cap at growing microtubule ends. *Cell* **149**:371–382. DOI: <https://doi.org/10.1016/j.cell.2012.02.049>, PMID: 22500803
- McCoy AJ,** Grosse-Kunstleve RW, Adams PD, Winn MD, Storoni LC, Read RJ. 2007. Phaser crystallographic software. *Journal of Applied Crystallography* **40**:658–674. DOI: <https://doi.org/10.1107/S0021889807021206>, PMID: 19461840
- McIntosh JR,** O'Toole E, Morgan G, Austin J, Ulyanov E, Ataulkhanov F, Gudimchuk N. 2018. Microtubules grow by the addition of bent guanosine triphosphate tubulin to the tips of curved protofilaments. *The Journal of Cell Biology* **217**:2691–2708. DOI: <https://doi.org/10.1083/jcb.201802138>, PMID: 29794031
- Mejillano MR,** Barton JS, Nath JP, Himes RH. 1990. GTP analogues interact with the tubulin exchangeable site during assembly and upon binding. *Biochemistry* **29**:1208–1216. DOI: <https://doi.org/10.1021/bi00457a017>, PMID: 2108723
- Mickolajczyk KJ,** Geyer EA, Kim T, Rice LM, Hancock WO. 2019. Direct observation of individual tubulin dimers binding to growing microtubules. *PNAS* **116**:7314–7322. DOI: <https://doi.org/10.1073/pnas.1815823116>, PMID: 30804205
- Mitchison T,** Kirschner M. 1984a. Dynamic instability of microtubule growth. *Nature* **312**:237–242. DOI: <https://doi.org/10.1038/312237a0>, PMID: 6504138
- Mitchison T,** Kirschner M. 1984b. Microtubule assembly nucleated by isolated centrosomes. *Nature* **312**:232–237. DOI: <https://doi.org/10.1038/312232a0>
- Mittal R,** Ahmadian MR, Goody RS, Wittinghofer A. 1996. Formation of a transition-state analog of the ras GTPase reaction by Ras-GDP, Tetrafluoroaluminate, and GTPase-activating proteins. *Science* **273**:115–117. DOI: <https://doi.org/10.1126/science.273.5271.115>, PMID: 8658179
- Nawrotek A,** Knossow M, Gigant B. 2011. The determinants that govern microtubule assembly from the atomic structure of GTP-tubulin. *Journal of Molecular Biology* **412**:35–42. DOI: <https://doi.org/10.1016/j.jmb.2011.07.029>, PMID: 21787788
- Nogales E,** Downing KH, Amos LA, Löwe J. 1998. Tubulin and FtsZ form a distinct family of GTPases. *Nature Structural Biology* **5**:451–458. DOI: <https://doi.org/10.1038/nsb0698-451>, PMID: 9628483
- Nogales E,** Wang HW. 2006. Structural intermediates in microtubule assembly and disassembly: how and why? *Current Opinion in Cell Biology* **18**:179–184. DOI: <https://doi.org/10.1016/j.ceb.2006.02.009>, PMID: 16495041
- Oliva MA,** Cordell SC, Löwe J. 2004. Structural insights into FtsZ protofilament formation. *Nature Structural & Molecular Biology* **11**:1243–1250. DOI: <https://doi.org/10.1038/nsmb855>, PMID: 15558053
- Oosawa FA.** 1975. *Thermodynamics of the Polymerization of Protein*. New York and London: Academic Press.
- Padinhateeri R,** Kolomeisky AB, Lacoste D. 2012. Random hydrolysis controls the dynamic instability of microtubules. *Biophysical Journal* **102**:1274–1283. DOI: <https://doi.org/10.1016/j.bpj.2011.12.059>, PMID: 22455910

- Prota AE**, Bargsten K, Zurwerra D, Field JJ, Díaz JF, Altmann KH, Steinmetz MO. 2013a. Molecular mechanism of action of microtubule-stabilizing anticancer agents. *Science* **339**:587–590. DOI: <https://doi.org/10.1126/science.1230582>, PMID: 23287720
- Prota AE**, Magiera MM, Kuijpers M, Bargsten K, Frey D, Wieser M, Jaussi R, Hoogenraad CC, Kammerer RA, Janke C, Steinmetz MO. 2013b. Structural basis of tubulin tyrosination by tubulin tyrosine ligase. *The Journal of Cell Biology* **200**:259–270. DOI: <https://doi.org/10.1083/jcb.201211017>, PMID: 23358242
- Prota AE**, Bargsten K, Northcote PT, Marsh M, Altmann KH, Miller JH, Díaz JF, Steinmetz MO. 2014. Structural basis of microtubule stabilization by laulimalide and peloruside A. *Angewandte Chemie International Edition* **53**:1621–1625. DOI: <https://doi.org/10.1002/anie.201307749>, PMID: 24470331
- Prota AE**, Setter J, Waight AB, Bargsten K, Murga J, Diaz JF, Steinmetz MO. 2016. Pironetin binds covalently to α cys316 and perturbs a major loop and Helix of α -Tubulin to inhibit microtubule formation. *Journal of Molecular Biology* **428**:2981–2988. DOI: <https://doi.org/10.1016/j.jmb.2016.06.023>, PMID: 27395016
- Rai A**, Liu T, Glauser S, Katrukha EA, Estévez-Gallego J, Rodríguez-García R, Fang W-S, Díaz JF, Steinmetz MO, Altmann K-H, Kapitein LC, Moores CA, Akhmanova A. 2019. Taxanes convert regions of perturbed microtubule growth into rescue sites. *Nature Materials* **13**:6. DOI: <https://doi.org/10.1038/s41563-019-0546-6>
- Ravelli RBG**, Gigant B, Curmi PA, Jourdain I, Lachkar S, Sobel A, Knossow M. 2004. Insight into tubulin regulation from a complex with colchicine and a stathmin-like domain. *Nature* **428**:198–202. DOI: <https://doi.org/10.1038/nature02393>
- Rice LM**, Montabana EA, Agard DA. 2008. The lattice as allosteric effector: structural studies of alpha- and gamma-tubulin clarify the role of GTP in microtubule assembly. *PNAS* **105**:5378–5383. DOI: <https://doi.org/10.1073/pnas.0801155105>, PMID: 18388201
- Schek HT**, Gardner MK, Cheng J, Odde DJ, Hunt AJ. 2007. Microtubule assembly dynamics at the nanoscale. *Current Biology* **17**:1445–1455. DOI: <https://doi.org/10.1016/j.cub.2007.07.011>, PMID: 17683936
- Seetapun D**, Castle BT, McIntyre AJ, Tran PT, Odde DJ. 2012. Estimating the microtubule GTP cap size in vivo. *Current Biology* **22**:1681–1687. DOI: <https://doi.org/10.1016/j.cub.2012.06.068>, PMID: 22902755
- Smith SJ**, Ma RK. 2002. *Preparation of GTPases for Structural and Biophysical Analysis*. Humana Press.
- Sternweis PC**, Gilman AG. 1982. Aluminum: a requirement for activation of the regulatory component of adenylate cyclase by fluoride. *PNAS* **79**:4888–4891. DOI: <https://doi.org/10.1073/pnas.79.16.4888>, PMID: 6289322
- Sugiyama T**, Miyashiro D, Takao D, Iwamoto H, Sugimoto Y, Wakabayashi K, Kamimura S. 2009. Quick shear-flow alignment of biological filaments for X-ray fiber diffraction facilitated by methylcellulose. *Biophysical Journal* **97**:3132–3138. DOI: <https://doi.org/10.1016/j.bpj.2009.09.041>, PMID: 20006950
- Sui H**, Downing KH. 2010. Structural basis of interprotofilament interaction and lateral deformation of microtubules. *Structure* **18**:1022–1031. DOI: <https://doi.org/10.1016/j.str.2010.05.010>, PMID: 20696402
- von Loeffelholz O**, Venables NA, Drummond DR, Katsuki M, Cross R, Moores CA. 2017. Nucleotide- and Mal3-dependent changes in fission yeast microtubules suggest a structural plasticity view of dynamics. *Nature Communications* **8**:2110. DOI: <https://doi.org/10.1038/s41467-017-02241-5>, PMID: 29235477
- Walker RA**, Pryer NK, Salmon ED. 1991. Dilution of individual microtubules observed in real time in vitro: evidence that cap size is small and independent of elongation rate. *The Journal of Cell Biology* **114**:73–81. DOI: <https://doi.org/10.1083/jcb.114.1.73>, PMID: 2050742
- Winn MD**, Ballard CC, Cowtan KD, Dodson EJ, Emsley P, Evans PR, Keegan RM, Krissinel EB, Leslie AG, McCoy A, McNicholas SJ, Murshudov GN, Pannu NS, Potterton EA, Powell HR, Read RJ, Vagin A, Wilson KS. 2011. Overview of the CCP4 suite and current developments. *Acta Crystallographica. Section D, Biological Crystallography* **67**:235–242. DOI: <https://doi.org/10.1107/S0907444910045749>, PMID: 21460441
- Wittinghofer A**. 1997. Signaling mechanistics: aluminum fluoride for molecule of the year. *Current Biology* **7**:R682–R685. DOI: [https://doi.org/10.1016/S0960-9822\(06\)00355-1](https://doi.org/10.1016/S0960-9822(06)00355-1), PMID: 9382787
- Zanic M**, Stear JH, Hyman AA, Howard J. 2009. EB1 recognizes the nucleotide state of tubulin in the microtubule lattice. *PLOS ONE* **4**:e7585. DOI: <https://doi.org/10.1371/journal.pone.0007585>, PMID: 19851462
- Zhang R**, Alushin GM, Brown A, Nogales E. 2015. Mechanistic origin of microtubule dynamic instability and its modulation by EB proteins. *Cell* **162**:849–859. DOI: <https://doi.org/10.1016/j.cell.2015.07.012>, PMID: 26234155
- Zhang R**, LaFrance B, Nogales E. 2018. Separating the effects of nucleotide and EB binding on microtubule structure. *PNAS* **115**:E6191–E6200. DOI: <https://doi.org/10.1073/pnas.1802637115>, PMID: 29915050